

# Ctrl-GenAug: Controllable Generative Augmentation for Medical Sequence Classification

Xinrui Zhou, Yuhao Huang, Haoran Dou, Shijing Chen, Ao Chang, Jia Liu, Weiran Long, Jian Zheng, Erjiao Xu, Jie Ren, Ruobing Huang, Jun Cheng, Wufeng Xue, and Dong Ni, *Member, IEEE*

**Abstract**—In the medical field, the limited availability of large-scale datasets and labor-intensive annotation processes hinder the performance of deep models. Diffusion-based generative augmentation approaches present a promising solution to this issue, having been proven effective in advancing downstream medical recognition tasks. Nevertheless, existing works lack sufficient semantic and sequential steerability for challenging video/3D sequence generation, and neglect quality control of noisy synthesized samples, resulting in unreliable synthetic databases and severely limiting the performance of downstream tasks. In this work, we present *Ctrl-GenAug*, a novel and general generative augmentation framework that enables highly semantic- and sequential-customized sequence synthesis and suppresses incorrectly synthesized samples, to aid medical sequence classification. Specifically, we first design a multimodal conditions-guided sequence generator for controllably synthesizing diagnosis-promotive samples. A sequential augmentation module is integrated to enhance the temporal/stereoscopic coherence of generated samples. Then, we propose a noisy synthetic data filter to suppress unreliable cases at semantic and sequential levels. Extensive experiments on 3 medical datasets, using 11 networks trained on 3 paradigms, comprehensively analyze the effectiveness and generality of *Ctrl-GenAug*, particularly in underrepresented high-risk populations and out-domain conditions.

**Index Terms**—Classification, Controllable Generative Augmentation, Medical Sequence Synthesis, Diffusion Model.

## I. INTRODUCTION

**D**YNAMIC information in medical imaging (e.g., video sequences) plays a vital role in clinical diagnosis. Recent deep learning-based classifiers have shown the ability to improve the diagnostic accuracy of different diseases [1],

X. Zhou, Y. Huang, S. Chen, A. Chang, R. Huang, J. Cheng, W. Xue, and D. Ni are with the National-Regional Key Technology Engineering Laboratory for Medical Ultrasound, School of Biomedical Engineering, Shenzhen University Medical School, Shenzhen University, Shenzhen, China, the Medical UltraSound Image Computing (MUSIC) Lab, Shenzhen University, Shenzhen, China, and also with the Marshall Laboratory of Biomedical Engineering, Shenzhen University, Shenzhen, China.

H. Dou is with the School of Computing, University of Leeds, UK, and also with the Department of Computer Science, School of Engineering, University of Manchester, UK.

J. Liu, W. Long, and J. Ren are with The Third Affiliated Hospital of Sun Yat-sen University, Guangzhou, China.

J. Zheng is with the Longgang District People's Hospital of Shenzhen, The Second Affiliated Hospital of The Chinese University of Hong Kong, Shenzhen, China.

E. Xu is with The Eighth Affiliated Hospital of Sun Yat-sen University, Shenzhen, China.

W. Xue and D. Ni are the corresponding authors (xuewf@szu.edu.cn, nidong@szu.edu.cn).

X. Zhou and Y. Huang contributed equally to this work.

[2]. Despite rapid advancements, the performance of current advanced solutions is still limited by several issues: 1) The scarcity of dynamic clinical cases, coupled with the high annotation cost, limits data availability; 2) Imbalanced data distribution, driven by the rarity of high-risk positive cases, skews model training; 3) Deep models are prone to brittle performance degradation when tested on out-domain data, e.g., cases from different medical centers [3], [4]. This risk presents a significant obstacle to deploying models in real-world medical settings. To address these issues, there is growing interest in generative augmentation paradigms, which employ advanced generative models to synthesize medical samples, thereby augmenting relevant diagnostic tasks.

Denosing diffusion probabilistic models (DDPMs), which utilize explicit likelihood estimation and a progressive sampling process for data synthesis, have more well-established mathematical explanations and abilities to achieve stable, controllable, and diverse synthesis than previous generative methods like generative adversarial networks (GANs) [5]–[7]. Diffusion models have garnered remarkable success in several natural image fields, including static image generation [8], [9], video synthesis [10]–[17], video editing [18]–[20], and image animation [21], [22]. Recently, researchers have explored high-fidelity medical sequence synthesis by applying the above approaches within the medical field [23], [24].

Most recently, pioneers deeply investigated the impact of the diffusion-based generative augmentation scheme on solving data scarcity [7], [25] and domain generalization [25] issues in diagnostic tasks. However, they failed to fully ensure the reliability of synthetic medical images for classification due to limited semantic steerability and absent quality control over the generated images. Moreover, their techniques focus on image-level synthesis rather than sequence-level synthesis, which is crucial for medical modalities like MRI, ultrasound (US), etc [7]. Thus, our study plans to devise a diagnosis-reliable controllable generative augmentation framework to facilitate accurate and robust medical sequence classification.

Intuitively, building customized, high-fidelity, and sequentially coherent synthetic medical databases, and effectively utilizing them, is essential for enhancing sequence recognition. However, this task presents several challenges. First, lesions (Fig. 1(a-b)) or structures (Fig. 1(c)) of the same disease category exhibit large visual variances (e.g., shapes, intensities, positions, etc). This may confuse diffusion learning seriously, thus causing uncontrollable and unreliable generation. Second,

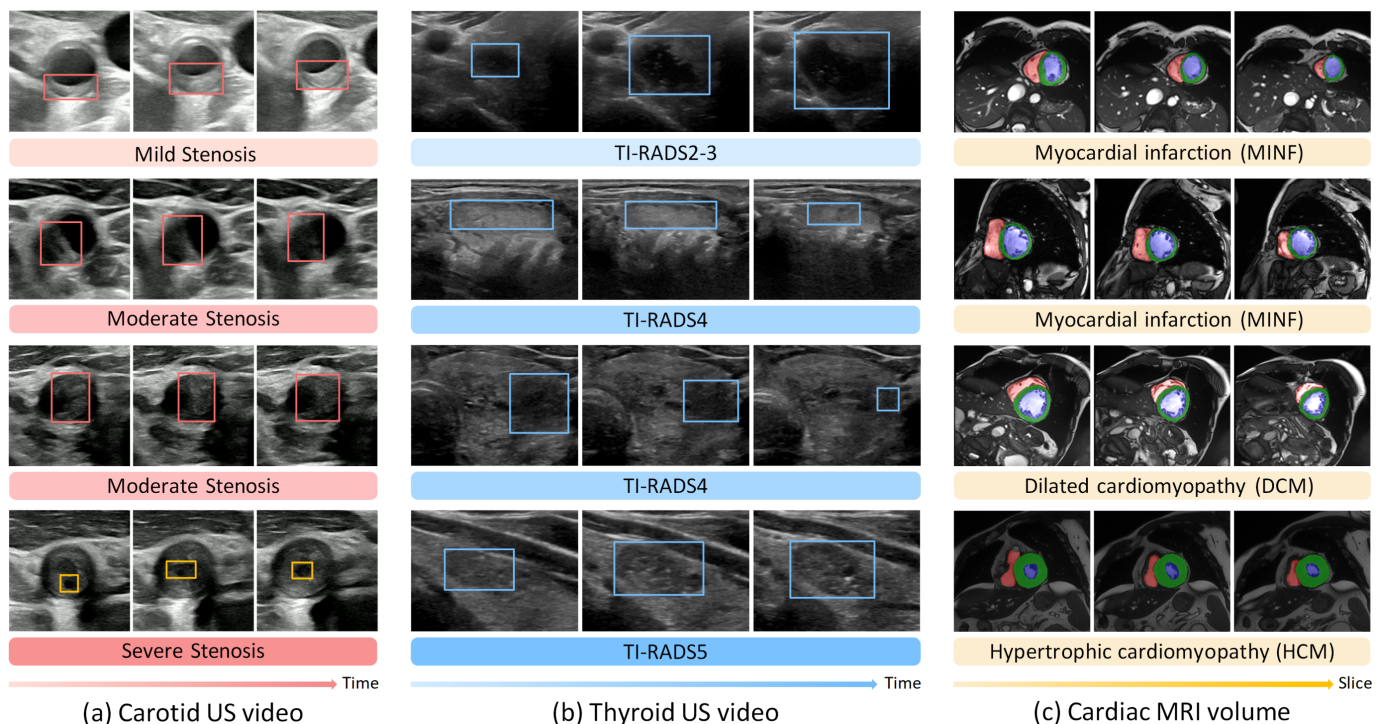


Fig. 1. Datasets description: (a) Carotid US videos with various stenosis gradings. Red and yellow boxes represent plaques and residual lumens, respectively. (b) Thyroid US videos with different TI-RADS levels, where blue boxes indicate nodules. (c) Cardiac MRI volumes with distinct diseases. Three key anatomical structures associated with diagnosis are highlighted with masks, including the left ventricle (blue), myocardium (green), and right ventricle (red).

artifacts and noises (e.g., US speckle noise) may prevent models from accurately perceiving vital anatomical targets, hindering the synthesis of high-fidelity sequences. Third, the complex dynamic changes (Fig. 1(a-b)) and the varying sizes of anatomical regions (Fig. 1(c)) challenge the coherence of synthesized sequences. The fourth challenge lies in the domain gap between synthetic and real samples, where achieving real-domain customization is crucial for effectively utilizing synthetic samples in downstream learning [26]. Lastly, even a well-designed sequence generator cannot always guarantee high-quality synthesis due to random sampling, and unsatisfactory synthetic samples may negatively impact subsequent classifier learning. In summary, from model- and data-centric perspectives, the challenges of the task can be concluded as: 1) How can we design the generator architecture to achieve satisfactory sequence synthesis? 2) How can we discriminatively filter out potentially harmful synthetic samples?

In this work, we propose a novel controllable generative augmentation framework, named *Ctrl-GenAug*, to facilitate medical sequence classification tasks on different organs and modalities. Concretely, *Ctrl-GenAug* synthesizes customized, high-quality sequences using conditional diffusion models and applies quality control to the generated sequences, to supplement medical datasets and improve classification. This is a general method for enhancing medical sequence classification. We believe this is the first comprehensive study to analyze the impact of the controllable generative augmentation scheme on promoting multi-modal medical sequence classification. Our contributions are three-fold:

- We propose a multimodal conditions-guided sequence

generator to ensure controllable and high-fidelity synthesis. The introduced image prior serves as conditional guidance to empower the real-domain customization capacity. Moreover, we design a sequential augmentation module to promote dynamics modeling, thus improving the temporal or stereoscopic coherence of generated data.

- We introduce a noisy synthetic data filter to suppress harmful synthetic sequences at class semantics and sequential levels. By effectively reducing noise and enhancing the reliability of the synthetic databases, we can associate the synthetic samples with downstream tasks, thus better improving the classification performance.
- Comprehensive experiments on 3 medical datasets, with 11 downstream networks trained on 3 paradigms, show that our proposed framework can improve diagnostic performance, especially within underrepresented high-risk sets. *Ctrl-GenAug* also increases out-domain robustness, further indicating its practicality in clinical scenarios.

It is noted that the sequence generator extends our prior work presented at MICCAI [23], with significant improvements in controllability at both semantic and sequential levels. We highlight that customized semantics and consistent sequential dynamics are crucial for enhancing the learning capability of downstream classifiers. Hence, we incorporate attribute texts and class labels to provide fine-grained semantic guidance, while employing a computation-efficient motion field to enhance dynamic control. Besides, we propose a sequential augmentation module to further ensure the sequential consistency and smoothness of generated samples.

## II. RELATED WORKS

In this section, we briefly review the approaches for controllable sequence synthesis using diffusion models. Given the strong inter-slice association in 3D medical volumes [27], we treat them as video sequence data in our study and summarize related video-based methods. Finally, we deeply involve existing diffusion-based generative augmentation schemes.

### A. Controllable Video Synthesis with Diffusion Models

Diffusion models, a class of generative models, have recently attracted significant attention, especially text-to-video (T2V) synthesis [10], [11], [28], [29]. However, these methods did not achieve precise control over the visual appearance and dynamics of the synthesized video, resulting in limited practicality. To mitigate this issue, researchers have concentrated on incorporating multimodal conditions into T2V frameworks to guide controllable synthesis. Specifically, *AnimateDiff* [30] and *MoonShot* [31] introduced text and image conditions to facilitate the control of visual appearance. Most recently, several studies [19], [32], [33] achieved fine-grained spatial compositional control by integrating additional diverse conditions (i.e., sketch, mask, and depth sequences). Meanwhile, two spatial-sequential ( $S^2$ ) modeling strategies (fully attention layers [19] and  $S^2$  condition encoder [33]) were introduced to capture the dynamics of sequential conditions, promoting the inter-frame features interaction. Besides, dense optical flow [34] was adopted to control sequential consistency [35], [36]. The above methods have shown promising controllability in natural video synthesis. However, for medical synthesis, acquiring abundant dense annotations (e.g., mask sequences) as control signals is impractical and unaffordable. Additionally, medical videos have unique attributes compared with natural ones, such as blurred anatomical regions and complex structure variations. Hence, they may not suit the medical video synthesis tasks.

In the medical field, several diffusion-based methods have been proposed to generate photorealistic echocardiography videos using the conditional guidance of a single frame [37], ejection fractions [37], single semantic mask [38], [39], and single sketch image [23]. Zhou et al. [23] additionally leveraged mitral valve (MV) skeletons to control the complex motion trajectories of MV in the generated echocardiograms. Besides, Li et al. [24] proposed an approach to generate endoscopy videos that simulate clinical scenes by integrating a spatial-temporal transformer with 2D vision foundation model priors. However, the above methods may have the following drawbacks: unsteerable semantics due to the lack of attribute guidance (e.g., category or target shape), poor control over sequences, etc. Thus, they may be unsuitable for direct adoption in the generative augmentation tasks.

### B. Generative Augmentation with Diffusion Models

Synthetic data can effectively supplement traditional data augmentation (e.g., rotation) and provide diverse samples to help deep model training [7], [40]. Previous works have succeeded in utilizing synthetic data generated with diffusion models to enhance natural image classification [26], [41]–[43],

segmentation [44]–[46], and detection [47]. Recently, Singh et al. [48] performed an in-depth analysis of models trained with synthetic data across various robustness measures, and verified that they achieved good suitability in real-world settings.

To address data scarcity and promote diagnostic performance, the intelligent medical field has raised increasing interest in exploring diffusion-based generative augmentation for aiding different downstream diagnostic tasks [25], [49]–[53]. Luo et al. [7] marked the first focus on comprehensively analyzing the impact of their designed uncertainty-guided diffusion models on downstream diagnostic tasks. Nevertheless, current studies have two main limitations:

On the one hand, due to the lack of adequate semantic and sequential guidance during sampling, coupled with the absence of post-sampling quality control for generated samples, existing works could hardly fully ensure the reliability of synthetic databases for downstream disease recognition. For instance, it is desirable to embed descriptive text (e.g., lesion morphology) to provide more informative guidance associated with disease grading. Unlike previous solutions, we aim to develop a generative augmentation framework that enables highly semantic- and sequential-customized sequence synthesis and suppresses incorrectly synthesized samples to better facilitate downstream classifier learning.

On the other hand, few studies comprehensively explore the effect of generative models on downstream medical tasks, and they solely focus on image-level generation. Considering the value of dynamic information for clinical diagnosis, we concentrate on diagnosis-reliable sequence synthesis. This is more challenging than image-related works as synthetic data not only meets high-fidelity requirements but also ensures temporal or stereoscopic consistency and coherence for effectively promoting downstream  $S^2$  modeling capacity. A brief review of studies in the medical field utilizing diffusion models to promote downstream tasks can be found in the **Supplementary Material**.

## III. METHOD

### A. Model Overview

Fig. 2 shows the pipeline of using our proposed controllable generative augmentation framework to aid medical sequence classification. First, we propose a sequence generator that enables perceiving multiple semantic and sequential conditions to guide controllable and diverse generation. Then, an efficient noisy data filter is introduced to suppress unsatisfactory synthetic sequences. Last, the quality-controlled synthetic sequences and real ones will work together to improve the performance of arbitrary classifiers. To formulate customized, high-fidelity, and coherent synthetic databases to boost classification, we design the whole framework from model-centric, i.e., sequence generator (Secs. III-B, III-C, and III-D) and data-centric, i.e., data filter (Sec. III-E) perspectives.

### B. Basic Architecture of Sequence Generator

Fig. 3 shows the pipeline of our proposed sequence generator. It supports customized and high-quality medical sequence

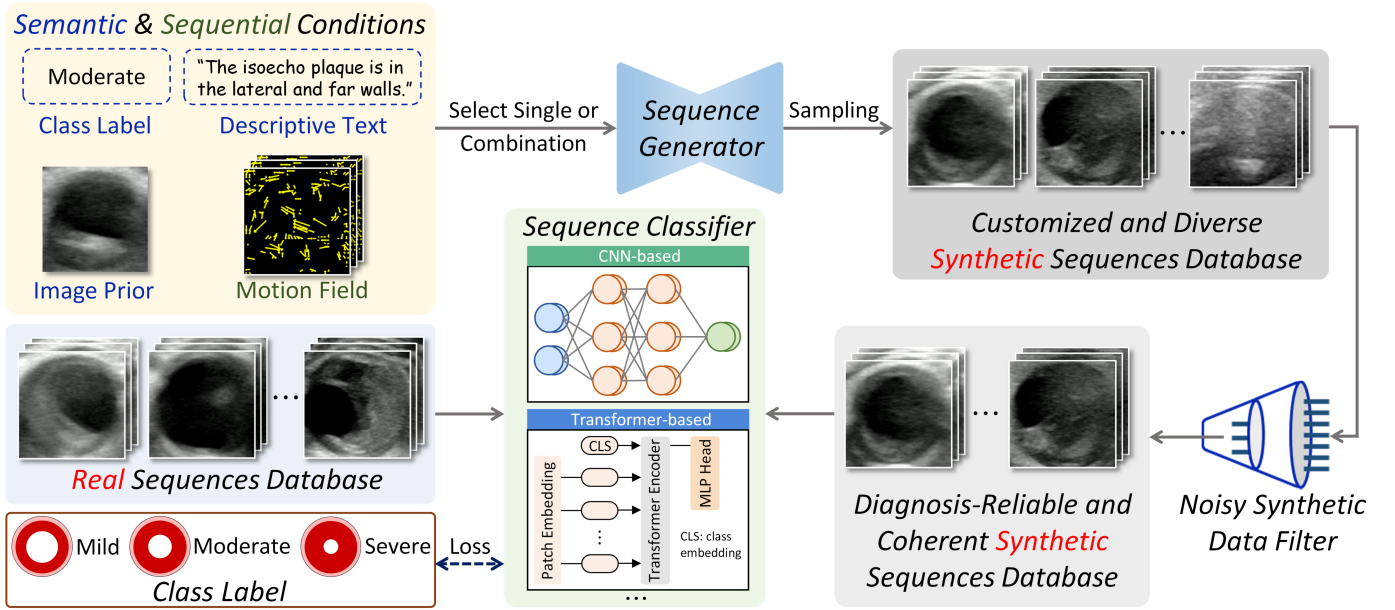


Fig. 2. Pipeline of using our proposed framework to facilitate medical sequence recognition, which can be worked with a variety of classifiers. Here, we use the carotid plaque US video sequence as an example to demonstrate the overall process.

generation via multimodal conditions. The generator is implemented with a two-stage training scheme. In the pretraining stage, it attends to high-fidelity *visual features learning* for controllable image synthesis. While in the finetuning stage, the domain-specific visual knowledge acquired from the previous stage is reused and focuses on *sequential patterns modeling* for customized sequence synthesis. During inference, given a single or combination of multimodal conditions as control signal inputs, high-quality and steerable sequence generation from Gaussian noise can work. We then provide a short background of video diffusion models in Sec. III-B1, followed by a detailed description of the basic architecture of our generator in Secs. III-B2 and III-B3.

1) *Preliminaries of Video DDPMs*: They are trained to learn complex video distribution by iteratively denoising corrupted inputs using pixel-space diffusion methods [54], [55]. Given a training video  $x_0 \sim q$  and let  $T$  the timestep, DDPMs first produce a sequence of noisy inputs via a diffusion process  $q(x_t|x_0, t)$ ,  $t \in 1, 2, \dots, T$ , which progressively adds Gaussian noise  $\epsilon \in \mathcal{N}(\mathbf{0}, \mathbf{I})$  to  $x_0$ . To ease the computational burden due to pixel-space training, video latent diffusion models [28] perform the diffusion process in latent space of a variational autoencoder [56] (VAE). The model is then trained to estimate the parameterized Gaussian transition  $p(x_{t-1}|x_t)$  via a denoising network  $\theta$ . Mathematically, the optimized objective can be a simplified variant of the variational lower bound:

$$\min_{\theta} \mathbb{E}_{z_0, \epsilon \sim \mathcal{N}(\mathbf{0}, \mathbf{I}), \mathbf{c}, t} \|\epsilon - \epsilon_{\theta}(z_t, \mathbf{c}, t)\|^2, \quad (1)$$

where  $z_0$  is the latent code of  $x_0$ .  $\epsilon_{\theta}$  and  $\epsilon$  represent the predicted and target noise, respectively. Here,  $\mathbf{c}$  denotes the (optional) control signal that the model can be conditioned on. For our generator,  $\mathbf{c}$  involves multimodal conditions including semantic and sequential ones.

2) *Factorized Learning of Visual Features and Sequential Patterns*: Developing a generator with pure 3D architecture design is an intuitive scheme for sequence synthesis [28]. However, it is very challenging to simultaneously learn visual features and sequential patterns due to the scarcity and complexity of medical data, while causing high training costs. To this end, we propose to factorize both learning by first pretraining a latent diffusion model (LDM) and then finetuning its sequence counterpart. In this way, the generator enables realistic sequence synthesis, while easing the training burden.

3) *2D-to-3D Model Inflation*: In the pretraining phase, we develop a 2D UNet [57] in LDM to predict noises for image synthesis. Referring to [13], we extend the 2D UNet to a 3D version via an inflation scheme to build the sequence LDM. Specifically, all the spatial convolution layers are inflated to pseudo-3D counterparts by expanding the kernels at the sequential dimension (e.g.,  $3 \times 3 \rightarrow 1 \times 3 \times 3$  kernel). Besides, we perform sequential insertion by adding sequential attention (SA) layers (see Fig. 3). Fig. 4(a) shows the principle of the SA mechanism, where each patch queries to those at the same spatial position and across frames/slices. This design encourages the generator to model the sequential patterns, while not significantly altering visual feature distribution baked in the LDM [31]. Overall, sequence LDM enables inheriting the rich visual concepts preserved in LDM and focusing on sequential pattern aggregation, making the model learning efficient.

### C. Multimodal Conditions Guidance

Sequence generators guided by a single condition (e.g., text) have the following drawbacks: 1) poor controllability and 2) sequential inconsistency. To solve these issues, we introduce multimodal conditions to guide our sequence generator for customized, realistic, and sequential-consistent synthesis.

### Multimodal Conditions-Guided Training

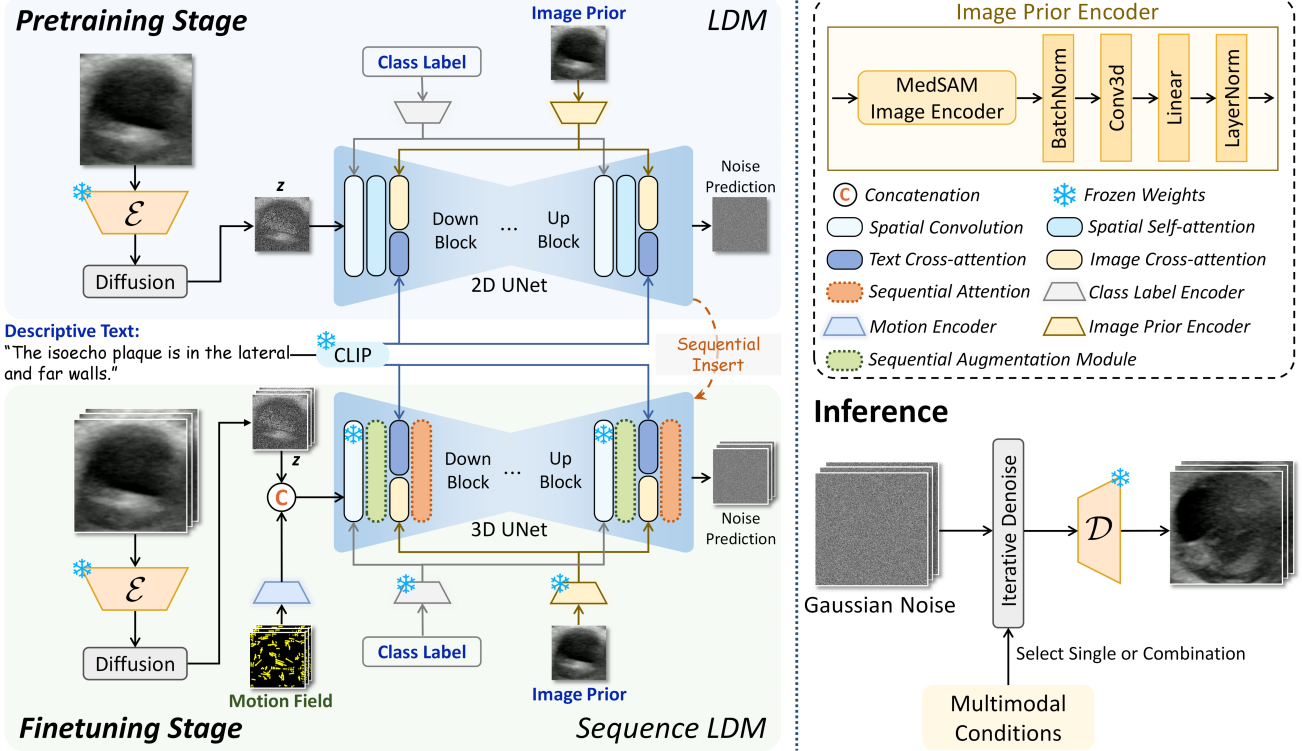


Fig. 3. Pipeline of our proposed sequence generator. The MedSAM image encoder [58] is adopted for domain-specific image prior feature extraction.

We consider four multimodal conditions to ensure comprehensive and accurate control over the sequence synthesis procedure (see Figs. 2-3). Specifically, these conditions are divided into semantic and sequential ones for visual appearance control and serial guidance, respectively. We highlight that our generator supports composable synthesis by allowing users to flexibly choose any single condition or composition during inference. This flexibility makes our generator particularly user-friendly, as it enables high-quality synthesis even when certain conditions are missing. Details are described below.

1) *Semantic Conditions for Visual Appearance Control:*

As shown in Fig. 3, the sequence generator exploits three semantic conditions to perform visual appearance control, thus achieving controllable and high-fidelity synthesis.

- *Descriptive Text:* It provides an intuitive indication of the coarse-grained semantic concepts of sequences. In our implementation, we pre-align the visual and textual features by finetuning the widely used CLIP model [59] using our medical datasets to mitigate the large gap between them. Then, semantic information of texts can feasibly query relevant medical visual patterns, thus easing subsequent training. Similar to [8], the text guides the generator via cross-attention layers.

- *Class Label:* Generating medical data with the expected disease class is crucial for enhancing downstream classification, particularly improving the diagnostic accuracy of underrepresented high-risk sets. Thus, we propose encouraging the model to focus on the grading signal. Specifically, rather than merging the class label with descriptive text, we treat it as a separate tag to directly provide disease-specific guidance,

as merging with text may dilute the class signal. We further propose a dedicated insertion method for this purpose. First, similar to the timestep embedding process [8] in diffusion models, we adopt a class label encoder composed of a label discretization layer and an embedding layer to obtain its embeddings. The addition between the timestep and class label embeddings is then input to the spatial convolution layer in each UNet block for visual appearance control.

- *Image Prior:* Merely using the above conditions faces challenges of insufficient semantic control and an inevitable domain gap between real and synthetic sequences, constraining the capability of generative augmentation. Hence, we introduce the first frame/slice of real-domain sequences as image priors to provide rich semantic guidance and yield real-domain style sequences. As image prior offers global semantics like texts, we align image prior features  $f_i$  extracted from image prior encoder (see Fig. 3) with text embeddings  $f_t$  generated by our medical data-specific CLIP text encoder for joint guidance. Specifically, motivated by [60], we replace the text-guided cross-attention layers in original UNet blocks with decoupled counterparts that handle texts and image priors in parallel and then merge the results by addition. The decoupled attention can be formulated as:

$$\begin{cases} \mathbf{Q}_g = W^{Q_g} f_g, \mathbf{K}_g = W^{K_g} f_g, \mathbf{V}_g = W^{V_g} f_g, g \in \{t, i\}, \\ Attention(\mathbf{Q}_g, \mathbf{K}_g, \mathbf{V}_g) = \sum_g \left[ \sigma \left( \frac{\mathbf{Q}_g \mathbf{K}_g^T}{\sqrt{d}} \mathbf{V}_g \right) \right], \end{cases} \quad (2)$$

where  $W^Q, W^K, W^V$  denote the trainable linear projection

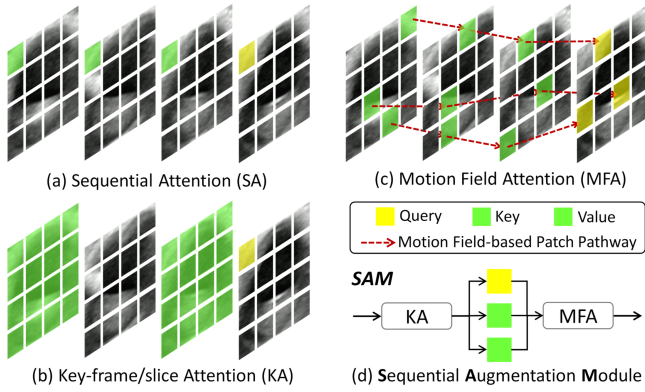


Fig. 4. Schematics of three attention mechanisms for sequential modeling (a-c) and our proposed sequential augmentation module in this study (d).

matrices.  $\mathbf{t}, \mathbf{i}$  represent text and image prior conditions.  $d$  denotes dimension of latent features.  $\sigma(\cdot)$ , softmax function.

2) *Sequential Condition for Serial Guidance*: Apart from perceiving visual concepts, modeling sequential knowledge is also important in sequence synthesis, with sequential cues playing a vital role in this process. Most existing methods [35], [36] adopted dense optical flow [34] to promote sequential dynamics modeling. However, optical flow extraction requires high computational demands [33]. Thus, we instead introduce computation-efficient *motion field* as a sequential condition in sequence LDM. It explicitly showcases the pixel-wise motions between adjacent frames/slices (see Figs. 2-3). In our approach, we first extract the motion fields of real sequences using a Python package [61]. Then, a motion encoder (see Fig. 3) receives the motion fields and produces motion features. Last, the features are concatenated with latent representations  $z$  from VAE along the channel dimension for serial guidance.

#### D. Sequential Augmentation Module

Solely equipping with SA layers and sequential cues in sequence LDM may present inadequate consistency and coherence across synthetic frames/slices. This issue may arise from insufficient sequential modeling of input noisy latents and motion fields, constrained by a small parameter space, overly burdening the SA layers. To solve the issue, we propose a sequential augmentation module (SAM) that enables the generator to more effectively model sequential dependencies. As shown in Fig. 4(d), SAM integrates two attention mechanisms in cascade for sequential augmentation.

1) *Key-frame/slice Attention*: The common spatial self-attention layers can lead to sequential inconsistency due to the lack of interaction across frames/slices. To augment *sequential consistency*, we introduce a key-frame/slice attention (KA) mechanism, where two selected key-frames/slices act as references to propagate  $S^2$  information throughout the sequence. Specifically, for any frame/slice, we select its previous and the first counterpart of the sequence as the references and transform spatial self-attention into KA, aiming to align the latent features  $z_l$  of the  $l$ -th frame/slice with  $z_1$  and  $z_{l-1}$ . We

obtain query from  $z_l$ , key and value features from  $z_1$  and  $z_{l-1}$ , and compute  $Attention(\mathbf{Q}, \mathbf{K}, \mathbf{V})$  using:

$$\mathbf{Q} = W^Q z_l, \mathbf{K} = W^K \{z_1, z_{l-1}\}, \mathbf{V} = W^V \{z_1, z_{l-1}\}, \quad (3)$$

where  $W^Q, W^K, W^V$  are initialized on the original spatial self-attention weights for inheriting the semantic perception capability of LDM in the finetuning stage.  $\{\cdot\}$  represents concatenation operation. It is highlighted that KA retains low computational complexity compared with full attention [19]. Please refer to Fig. 4(b) for a visual illustration.

2) *Motion Field Attention*: To further boost the *sequential coherence* of the generated sequences, we propose to reuse the motion field condition (refer to Sec. III-C2) by introducing a motion field attention (MFA) mechanism after KA. As shown in Fig. 4(c), MFA requires the patches to communicate with those in the same motion field-based pathway including itself, which eliminates flickers of the generated sequences to make the contents visually smooth. Inspired by [62], MFA is implemented in two steps: a) motion field-based patch pathway sampling and b) attention calculation. In **step 1**, we sample the patch pathways based on the  $m$ -scaled downsampled motion fields. Take a video sequence as an example, for a patch  $p_l$  on the  $l$ -th frame of a  $f$ -frame video, the *path* can be derived from the motion field. Since the sampling procedure inevitably generates multiple pathways for the same patch, we randomly sample a pathway to ensure its uniqueness to which each patch belongs. In this setting, let  $H, W$  the height and width of the input video frame, then the size of the pathway set after sampling equals  $\frac{H \times W}{m^2} \times f$ . In **step 2**, we calculate  $Attention(\mathbf{Q}, \mathbf{K}, \mathbf{V})$  with:

$$\mathbf{Q} = z_{p_l}, \mathbf{K} = \mathbf{V} = z_{path}, \quad (4)$$

where  $z_{path}$  represents the latent features of patches on the *path*, as follows:

$$z_{path} = [z_{p_0}, z_{p_1}, \dots, z_{p_l}, \dots, z_{p_{f-1}}, z_{p_f}]. \quad (5)$$

The output of KA is directly fed into MFA without being handled by the query, key, and value projection functions. Hence, MFA can comfortably decrease extra computation.

#### E. Noisy Synthetic Data Filter

We use the proposed sequence generator to constitute the synthetic samples set. Concretely, assuming there are  $n$  training clips in the target dataset, with a bank of conditions derived from each clip, we synthesize a group of clips guided by each conditions bank. Eventually, we obtain  $n$  groups of clips to form our synthetic sample set, with a total of  $N$  clips. Although visually realistic and smooth (good cases, Fig. 5), sequence synthesis may still suffer from class semantics misalignment, cross-frame/slice inconsistency or over-consistency (i.e., almost static clip), and inter-clip similarity. For instance, in Fig. 5(e), the synthesized carotid clip category is wrong, which should be moderate rather than mild. In Fig. 5(f), the generated clip includes abrupt changes in anatomical

<sup>1</sup> $\ominus$  calculates inter-clip similarity (refer to Sec. III-E2).

---

**Algorithm 1** Noisy synthetic data filtering.

---

**Require:** synthetic samples set  $S$ , real data-trained classifier  $p$ .

- 1: # Stage 1: Class semantics misalignment filtering
- 2:  $S_1 = \emptyset$   $\triangleright$  synthetic samples set obtained after stage 1
- 3: **for**  $i \in \{1, \dots, n\}$  **do**
- 4:    $c \leftarrow$  class in the conditions bank of the group  $S[i]$
- 5:    $l_x = -\sum \text{clog}\sigma(p(S[i][x]))$   $\triangleright$  loss of the sample indexed  $x$
- 6:    $L_c = \frac{1}{M} \sum_{x=1}^M l_x$   $\triangleright$  noise identification threshold  $\triangleright M$  clips in the group
- 7:   **for**  $x \in \{1, \dots, M\}$  **do**
- 8:     **if**  $l_x > L_c$  **then**
- 9:        $\text{continue}$
- 10:     **else**
- 11:        $S_1 \leftarrow S_1 \cup \{S[i][x]\}$   $\triangleright$  save less noisy sample
- 12:     **end if**
- 13:   **end for**
- 14: **end for**
- 15: **return**  $S_1$   $\triangleright$  with  $n_1 (< n)$  groups totaling  $N_1 (< N)$  clips
- 16: # Stage 2: Inner-sequence filtering
- 17:  $S_2 = \emptyset$   $\triangleright$  synthetic samples set obtained after stage 2
- $A = \{A_1, \dots, A_N\}$   $\triangleright$  VAE-Seq values set of  $S$
- $B = \{B_1, \dots, B_{N_1}\}$   $\triangleright$  VAE-Seq values set of  $S_1$
- 18:  $t_l, t_h \leftarrow \text{KMeans}(A, K = 4)$   $\triangleright$  boundary thresholds
- 19: **for**  $j \in \{1, \dots, N_1\}$  **do**
- 20:   **if**  $B_j \geq t_l$  &  $B_j \leq t_h$  **then**
- 21:      $S_2 \leftarrow S_2 \cup \{y_j | y_j \in S_1\}$   $\triangleright$  save gentle dynamic sample
- 22:   **else**
- 23:      $\text{continue}$
- 24:   **end if**
- 25: **end for**
- 26: **return**  $S_2$   $\triangleright$  with  $n_2 (< n_1)$  groups totaling  $N_2 (< N_1)$  clips
- 27: # Stage 3: Inter-sequence filtering
- 28:  $S_3 = \emptyset$   $\triangleright$  synthetic samples set obtained after stage 3
- 29: **for**  $k \in \{1, \dots, n_2\}$  **do**
- 30:    $S_3 \leftarrow S_3 \cup S_2[k][1]$
- 31:   **for**  $q \in \{2, \dots, M'\}$  **do**  $\triangleright M'$  clips in the group  $S_2[k]$
- 32:     **if**  $\forall z \in S_3, \Theta^1(S_2[k][q], z) < 98$  **then**
- 33:        $S_3 \leftarrow S_3 \cup S_2[k][q]$   $\triangleright$  save diverse sample
- 34:     **else**
- 35:        $\text{continue}$
- 36:     **end if**
- 37:   **end for**
- 38: **end for**
- 39: **return**  $S_3$   $\triangleright$  final synthetic database for downstream training

---

structures. Hence, blindly using all synthetic clips for classifier learning will significantly cause a performance drop due to noisy samples. Our work proposes a noisy synthetic data filter to adaptively remove harmful generated clips at class semantics and sequential levels, as illustrated in Algorithm 1. This can also link the synthetic data to downstream tasks, thus potentially achieving a higher performance upper bound.

1) *Class Semantics Misalignment Filtering:* This scheme is designed to filter the generated clips whose visual contents mismatch the corresponding class labels. Motivated by anomaly detection [63], we consider that such noisy synthetic samples will produce large losses if fed into a powerful classifier trained on real ones. Hence, a loss threshold can be set to identify and filter the anomalistic clips. Specifically, we first adopt a well-trained classifier in the real data domain to calculate case-wise cross-entropy loss values  $\{l_x\}_{x=1}^M$  based on corresponding category  $c$  for all synthetic clips in each group. Then, we set the average loss as the noise identification threshold of  $c$ . Last, we conduct class semantics misalignment

filtering at the group level. If the loss of a synthetic clip with  $c$  exceeds the threshold  $L_c$ , it will be viewed as a noisy sample and excluded from the synthetic pool.

2) *Sequential Filtering:* This strategy aims to filter noisy samples at a) inner-sequence and b) inter-sequence levels. *For a)*, we screen out synthetic clips with gentle dynamic, avoiding those that are either inconsistent or over-consistent affecting downstream learning. Specifically, we retain a synthetic clip whose cross-frame/slice consistency falls in a pre-computed range. It is determined by K-means clustering [64] based on the cross-frame/slice consistency of all synthetic clips. To assess the video sequence consistency, [33] tends to use CLIP [59] image embeddings to compute the average cosine similarity across consecutive frames. However, this method leads to inadequate evaluation due to the usage of limited informative CLIP embeddings. To resolve the problem, we propose a metric termed VAE-Seq that utilizes latent embeddings from pretrained VAE, instead of deriving embeddings from CLIP space, to assess cross-frame/slice consistency. Therefore, with the higher dimension of latents (e.g.,  $4 \times 32 \times 32$  for input size  $256 \times 256$  compared to 768 in CLIP embeddings), VAE-Seq reflects an accurate evaluation using more fine-grained and informative features. *For b)*, we seek to diversify the samples in the synthetic set to prevent overfitting and avoid wasting computational resources in downstream training. To this end, we perform the inter-sequence filtering based on inter-clip similarity in each group, as shown in Algorithm 1. We quantify the inter-clip similarity by calculating the cosine distance of VAE latent embeddings between frame/slice pairs in two clips and averaging the obtained distance values.

### F. Evaluation

As a common practice, existing sequence synthesis works evaluate the synthetic quality by mostly using Fréchet Inception Distance (FID) [65] and Fréchet Video Distance (FVD) [66]. However, researchers have verified that these metrics do not consistently correlate with performance metrics on downstream tasks [7], [46]. To exhaustively evaluate the values of synthetic samples to downstream tasks, eleven popular classifiers are deployed for comparison with respect to diagnostic accuracy and area under the receiver operating characteristic curve (AUROC). Besides, we adopt the proposed VAE-Seq to assess the cross-frame/slice consistency (refer to Sec. III-E2). Moreover, we consider it crucial to evaluate the smoothness of generated clips. Motivated by [67], we quantify it using the proposed metric (termed Dynamic Smoothness), which is the mean absolute error between the reconstructed frames/slices from the interpolation model [68] and the original real ones.

## IV. EXPERIMENTS

In this section, we first comprehensively validated the effectiveness and generality of our method on three medical datasets, using eleven popular networks trained on three paradigms. We then tested the performance of our method in underrepresented high-risk sets and out-domain conditions. Last, we analyzed the contributions of our proposed multi-modal conditions guidance, sequential augmentation module,

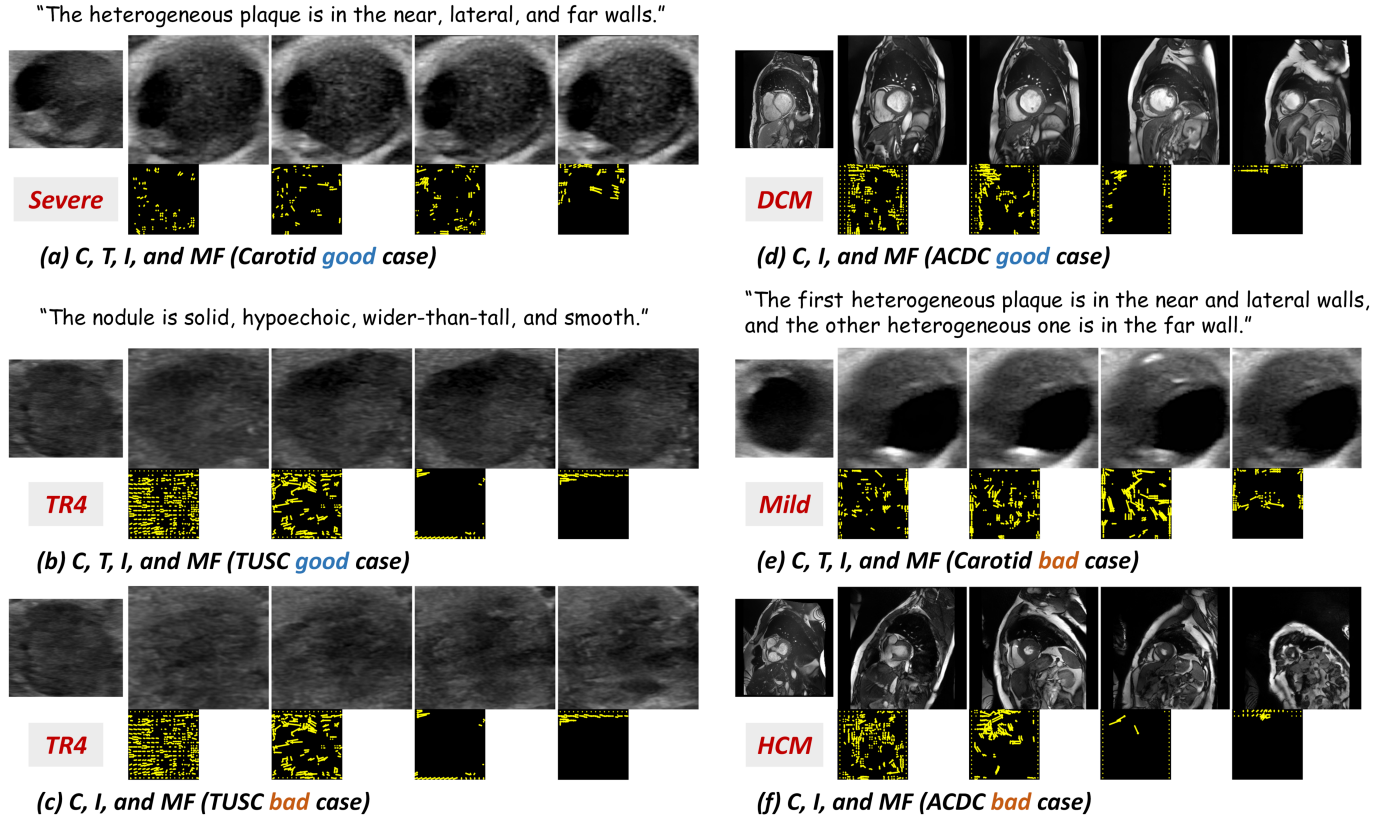


Fig. 5. Typical good and bad synthetic samples of three datasets using different banks of conditions. Conditional controls include class label (C), text (T), image prior (I), and motion field (MF). See more synthetic results in **Supplementary Material**.

and noisy synthetic data filter respectively, as well as the impacts of traditional and generative augmentations.

TABLE I  
EXPERIMENTAL DATASETS AND SETTINGS.

	Carotid	TUSC [69]	ACDC [70]
Patient	231	167	150
Clip	486	633	314
	Mild/Moderate/Severe	TI-RADS2-3/4/5	NOR/MINF/DCM/HCM/ARV
Class (train)	141/104/64	146/189/113	40/40/40/40/45
Class (test)	51/27/20	64/73/48	21/20/20/20/28
Class (OD)	37/24/18	-	-
<i>Training</i>			
Sequence generator	Downsampling rate of VAE(8)		T(1,000)
	AdamW(lr=1e-4)		lr scheduler(Cosine)
	Epochs(200)	Pretraining batch size(64)	Warm(500 iterations)
<i>Inference</i>			
Classifier-free guidance [71] factor(7.5)			
Eleven classifiers	Adam(lr=1e-4)		lr scheduler(Cosine)
	Traditional augmentations(Random Color/Move/Gaussian/Rotation/Flip)		Epochs(100) Batch size(8)

### A. Datasets and Settings

**Carotid dataset** was collected by three medical centers with approval from local institutional review boards, including a) The Third Affiliated Hospital of Sun Yat-sen University, b) Shenzhen Longgang District People’s Hospital, and c) The Eighth Affiliated Hospital of Sun Yat-sen University.

It consists of 273 US video sequences from 231 patients with carotid plaque-induced stenosis. The severity of carotid stenosis is graded into three stages, i.e., mild, moderate, and severe. We uniformly sampled several non-overlapping 8-frame clips from each sequence. The final dataset involved an in-domain (ID) subset (407 clips from 193 patients collected by Center (a)) and an out-domain (OD) subset (79 clips from 38 patients acquired from Center (b)-(c)). The ID/OD subset was randomly split into 309/39 and 98/40 clips for training and testing at the patient level. Each clip has up to two plaques and was labeled with stenosis grading and descriptive text by experienced sonographers using Pair annotation software package [72]. The text annotations indicated the plaque characteristics of echogenicity and location (see Fig. 2). We cropped the region of interest based on the pretrained carotid vessel detector [73] for easing the model learning.

**TUSC [69]** contains 192 thyroid US video sequences from 167 patients collected by the Stanford University Medical Center, with each including one nodule. Each sequence provided a TI-RADS level and nodule descriptors [74] (e.g., shape), the latter of which was used to form descriptive text. The TI-RADS level is ranging from 1 to 5. Considering the imbalanced distribution of TI-RADS levels, as suggested by the experienced sonographers, we rebuilt the dataset by removing the TI-RADS1 video sequence and combining the levels 2-3 sequences into a unified category named TI-RADS2-3. We uniformly sampled the sequences, obtaining 633 8-frame



clips, with 448 for training and 185 for testing. Each sampled clip inherited the same TI-RADS level and text as the original sequence. The bounding box of the nodule region for each frame was extracted by radiologists, similar to [75].

**ACDC** [70] includes 4D cardiac cine-MRI from 150 patients acquired at the University Hospital of Dijon. The patients were evenly divided into five classes: normal patients (NOR), myocardial infarction (MINF), dilated cardiomyopathy (DCM), hypertrophic cardiomyopathy (HCM), and abnormal right ventricle (ARV). We first extracted 3D volume sequences at end-systole and diastole phases from each case and assigned corresponding classes. Then, the 8-slice clips were uniformly sampled from each sequence along the slice axis. Finally, 205 and 109 clips were constructed for training and testing. Text prompts were set to empty strings during generator training.

Table I presents a detailed description of experimental datasets and settings. Using all available conditions, we synthesized 300 clips per category for the ACDC dataset and 500 clips per class for others. All frames/slices were resized to  $256 \times 256$ . By default, we set  $m=8$  for the MFA mechanism. For the sequence generator, the pretraining LDM was built upon Stable Diffusion [8] and initialized with the public weights<sup>2</sup>. During sequence LDM finetuning, we updated the parameters of SAM, SA layers, and motion encoder. We further refined the text- and image prior-sequence alignment by keeping the query projection matrices in cross-attention layers trainable. During generator training, we employed the multimodal conditions joint training strategy [76]. This allows users to flexibly select any single condition or combination during sampling, without finetuning the model for each specific combination. Motivated by [46], we adopted three paradigms to explore the impacts of the synthetic samples for downstream classifiers. **Baseline**: merely trained with real clips. **Real-finetune**: initially pretrained with synthetic clips and then finetuned with real ones. **Joint-train**: real clips were first over-sampled to match the number of synthetic clips, the classifier was then trained on the real-synthetic mixed set. All classification experiments were conducted on MMAAction2 [77] except for FTC [78] and CSG-3DCT [1].

### B. Generative Augmentation-based Sequence Classification

We utilized *Real-finetune* and *Joint-train* paradigms to integrate real and synthetic clips for downstream multi-class sequence classification training. The efficacy of our framework was fully validated across three medical datasets using eleven common classifiers. To demonstrate the generalizability of *Ctrl-GenAug*, the selected networks involve 3D CNN, transformer, and CNN-Transformer hybrid designs, which specialize in capturing local, global, and mixed features, respectively.

Table II compares the average performance (i.e., accuracy and AUROC) on different training paradigms across a wide range of sequence classifiers, including **five** CNN-based classic models, **three** transformer-based models, and **three** CNN-Transformer hybrid-based methods. It is evident that the performance ceiling of existing popular models, from simple CNN-based to complex CNN-Transformer hybrids, can

be further elevated using synthetic samples obtained from our proposed framework, under *Real-finetune* and *Joint-train* paradigms. On the carotid dataset, the accuracy/AUROC can be most boosted by 5.44%/0.077 and 6.80%/0.086 through *Real-finetune* and *Joint-train* paradigms, respectively. Due to high intra-class variations in TUSC, the baseline exhibits visibly inferior results, with an average accuracy of 62.42% compared to other datasets. However, it can be seen from Table II that samples synthesized by *Ctrl-GenAug* make significant contributions and enhance the classification performance to an acceptance level. Among all the classifiers, CSN harvests the largest performance gain, which is non-trivially enhanced by 5.41%/0.061 and 3.61%/0.040 accuracy/AUROC under *Real-finetune* and *Joint-train* paradigms, respectively. Notably, for ACDC, the overall performance improvement remains significant even with a high baseline. For instance, CSG-3DCT is boosted from 87.16%→88.63% (+1.47%) accuracy and from 0.797→0.820 (+0.023) AUROC under the *Joint-train* practice. Extensive experimental results show that synthetic sample sets produced by *Ctrl-GenAug* can be powerful data engines to enhance various diagnostic tasks in medical sequence analysis.

### C. Improved Diagnosis in Underrepresented High-risk Sets

We tested the effectiveness of *Ctrl-GenAug* by evaluating the diagnostic performance in underrepresented high-risk situations using our carotid dataset. In our study, *underrepresented* represents the tail data with small amounts (i.e., moderate&severe), and *overrepresented* defines mild data with sufficient amounts. To build a class-biased dataset, we skewed the real training dataset by randomly sampling 25% clips from each high-risk class (moderate&severe) in the underrepresented sets. We leveraged *Ctrl-GenAug* to expand the clips of each high-risk class to match the number of the low-risk class (mild), resulting in an augmented dataset. Four downstream networks were trained on the augmented dataset with *Joint-train* paradigm, and six metrics were used for class-level evaluation, including sensitivity, specificity, accuracy, F1-score, precision, and AUROC.

Fig. 6 quantitatively compares the carotid stenosis diagnostic performance of underrepresented high-risk sets on *Baseline* and *Joint-train* paradigms. It shows that *Baseline* performs poorly on underrepresented high-risk sets, especially in terms of sensitivity (average 18.52% in moderate and 36.25% in severe sets). In comparison, the classifiers can be greatly enhanced by jointly training with synthetic samples (e.g., *SlowFast*: 11.11%→44.44% sensitivity on the moderate set).

We also provided the category-level analysis, and summarized the average F1 scores across four classifiers for a global observation and conclusion. Specifically, *Baseline* reached 69.92%, 25.92%, and 43.44% average F1 scores for mild, moderate, and severe cases, respectively. The F1 performance of *Joint-train* in these three categories was 82.44%, 52.73%, and 60.40%. We found that well-designed classifiers jointly trained on synthetic samples from *Ctrl-GenAug* and real ones, can effectively close diagnostic performance gaps between overrepresented (i.e., mild) and underrepresented sets (i.e., moderate and severe) while improving the former ( $\sim 13\%$ ↑).

<sup>2</sup><https://huggingface.co/CompVis/stable-diffusion-v1-4>

TABLE II

DIAGNOSTIC PERFORMANCE COMPARISON USING ELEVEN CLASSIFIERS TRAINED ON *Baseline* (A), *Real-finetune* (B), AND *Joint-train* (C) PARADIGMS IN MULTI-ORGAN AND MULTI-MODAL DATASETS. "HYBRID", THE CLASSIFIER WITH CNN-TRANSFORMER DESIGN. ACC., ACCURACY (%).

Method	Backbone	Training Paradigm	Carotid				TUSC [69]				ACDC [70]			
			Acc.	$\Delta$	AUROC	$\Delta$	Acc.	$\Delta$	AUROC	$\Delta$	Acc.	$\Delta$	AUROC	$\Delta$
I3D [79]	CNN	A	79.59		0.737		60.72		0.559		83.49		0.733	
		B	85.03	$\uparrow 5.44$	0.813	$\uparrow 0.076$	65.41	$\uparrow 4.69$	0.611	$\uparrow 0.052$	87.16	$\uparrow 3.67$	0.795	$\uparrow 0.062$
		C	84.35	$\uparrow 4.76$	0.811	$\uparrow 0.074$	62.88	$\uparrow 2.16$	0.578	$\uparrow 0.019$	85.32	$\uparrow 1.83$	0.762	$\uparrow 0.029$
R(2+1)D [80]	CNN	A	82.99		0.781		63.96		0.595		83.85		0.737	
		B	83.67	$\uparrow 0.68$	0.797	$\uparrow 0.016$	64.68	$\uparrow 0.72$	0.601	$\uparrow 0.006$	85.69	$\uparrow 1.84$	0.769	$\uparrow 0.032$
		C	85.04	$\uparrow 2.05$	0.804	$\uparrow 0.023$	65.41	$\uparrow 1.45$	0.610	$\uparrow 0.015$	85.69	$\uparrow 1.84$	0.771	$\uparrow 0.034$
SlowFast [81]	CNN	A	80.95		0.742		62.88		0.579		81.65		0.702	
		B	81.63	$\uparrow 0.68$	0.770	$\uparrow 0.028$	65.76	$\uparrow 2.88$	0.609	$\uparrow 0.030$	86.05	$\uparrow 4.40$	0.772	$\uparrow 0.070$
		C	84.35	$\uparrow 3.40$	0.811	$\uparrow 0.069$	65.41	$\uparrow 2.53$	0.609	$\uparrow 0.030$	83.85	$\uparrow 2.20$	0.742	$\uparrow 0.040$
CSN [82]	CNN	A	80.27		0.757		61.80		0.570		85.69		0.765	
		B	84.35	$\uparrow 4.08$	0.784	$\uparrow 0.027$	67.21	$\uparrow 5.41$	0.631	$\uparrow 0.061$	87.15	$\uparrow 1.46$	0.794	$\uparrow 0.029$
		C	87.07	$\uparrow 6.80$	0.843	$\uparrow 0.086$	65.41	$\uparrow 3.61$	0.610	$\uparrow 0.040$	88.62	$\uparrow 2.93$	0.814	$\uparrow 0.049$
TPN [83]	CNN	A	82.99		0.784		64.32		0.602		83.85		0.735	
		B	87.76	$\uparrow 4.77$	0.856	$\uparrow 0.072$	66.85	$\uparrow 2.53$	0.633	$\uparrow 0.031$	85.32	$\uparrow 1.47$	0.764	$\uparrow 0.029$
		C	85.71	$\uparrow 2.72$	0.823	$\uparrow 0.039$	65.41	$\uparrow 1.09$	0.609	$\uparrow 0.007$	84.95	$\uparrow 1.10$	0.756	$\uparrow 0.021$
TimeSformer [84]	Transformer	A	77.55		0.721		65.41		0.614		72.48		0.562	
		B	80.95	$\uparrow 3.40$	0.753	$\uparrow 0.032$	66.49	$\uparrow 1.08$	0.626	$\uparrow 0.012$	76.51	$\uparrow 4.03$	0.626	$\uparrow 0.064$
		C	79.59	$\uparrow 2.04$	0.730	$\uparrow 0.009$	66.49	$\uparrow 1.08$	0.618	$\uparrow 0.004$	77.62	$\uparrow 5.14$	0.642	$\uparrow 0.080$
MViTv2 [85]	Transformer	A	74.15		0.663		59.64		0.543		77.98		0.642	
		B	78.91	$\uparrow 4.76$	0.740	$\uparrow 0.077$	63.96	$\uparrow 4.32$	0.596	$\uparrow 0.053$	78.72	$\uparrow 0.74$	0.653	$\uparrow 0.011$
		C	76.87	$\uparrow 2.72$	0.701	$\uparrow 0.038$	62.17	$\uparrow 2.53$	0.568	$\uparrow 0.025$	80.18	$\uparrow 2.20$	0.680	$\uparrow 0.038$
VideoSwin [86]	Transformer	A	79.59		0.732		58.92		0.535		74.31		0.572	
		B	83.67	$\uparrow 4.08$	0.789	$\uparrow 0.057$	61.08	$\uparrow 2.16$	0.551	$\uparrow 0.016$	79.45	$\uparrow 5.14$	0.663	$\uparrow 0.091$
		C	83.67	$\uparrow 4.08$	0.776	$\uparrow 0.044$	61.44	$\uparrow 2.52$	0.562	$\uparrow 0.027$	77.62	$\uparrow 3.31$	0.632	$\uparrow 0.060$
UniFormerV2 [87]	Hybrid	A	76.87		0.710		65.41		0.611		75.78		0.614	
		B	80.27	$\uparrow 3.40$	0.743	$\uparrow 0.033$	65.77	$\uparrow 0.36$	0.618	$\uparrow 0.007$	77.25	$\uparrow 1.47$	0.645	$\uparrow 0.031$
		C	81.63	$\uparrow 4.76$	0.760	$\uparrow 0.050$	66.13	$\uparrow 0.72$	0.617	$\uparrow 0.006$	77.61	$\uparrow 1.83$	0.637	$\uparrow 0.023$
FTC [78]	Hybrid	A	76.99		0.723		62.09		0.584		80.95		0.689	
		B	80.91	$\uparrow 3.92$	0.750	$\uparrow 0.027$	64.09	$\uparrow 2.00$	0.593	$\uparrow 0.009$	82.38	$\uparrow 1.43$	0.703	$\uparrow 0.014$
		C	81.80	$\uparrow 4.81$	0.758	$\uparrow 0.035$	65.66	$\uparrow 3.57$	0.614	$\uparrow 0.030$	84.38	$\uparrow 3.43$	0.718	$\uparrow 0.029$
CSG-3DCT [1]	Hybrid	A	84.35		0.812		61.44		0.571		87.16		0.797	
		B	87.07	$\uparrow 2.72$	0.831	$\uparrow 0.019$	63.96	$\uparrow 2.52$	0.590	$\uparrow 0.019$	88.62	$\uparrow 1.46$	0.819	$\uparrow 0.022$
		C	87.76	$\uparrow 3.41$	0.837	$\uparrow 0.025$	65.05	$\uparrow 3.61$	0.609	$\uparrow 0.038$	88.63	$\uparrow 1.47$	0.820	$\uparrow 0.023$

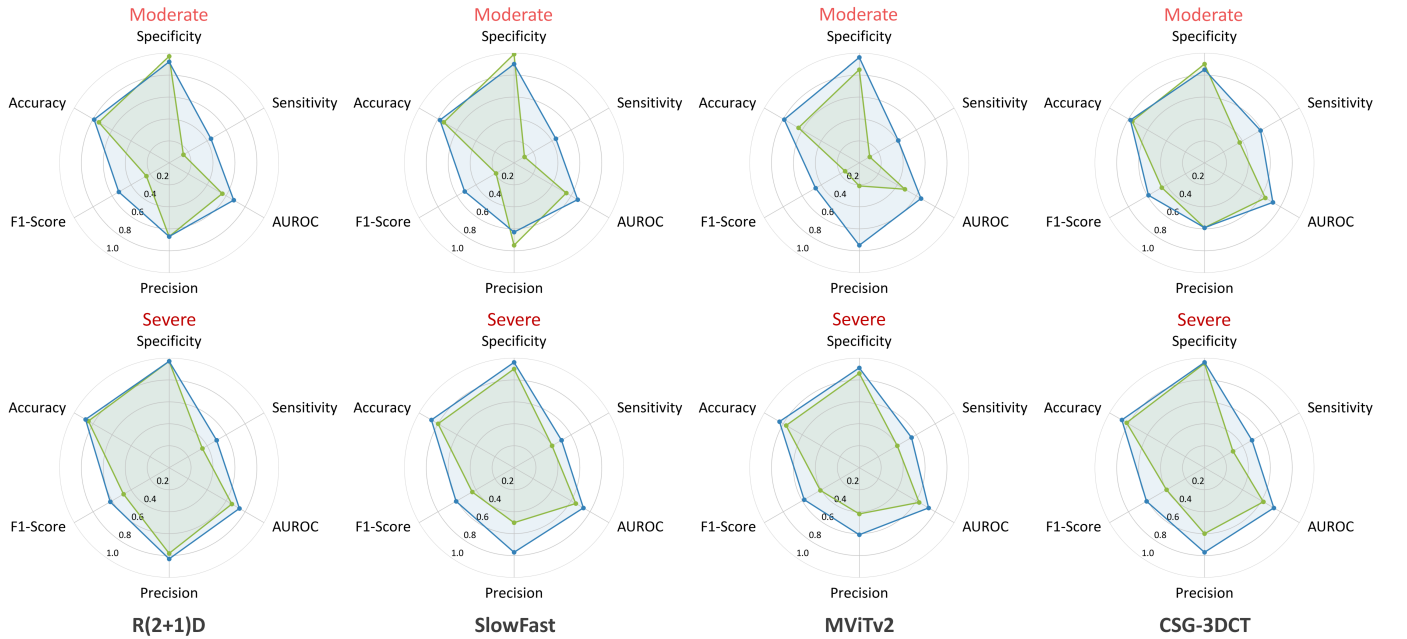


Fig. 6. Carotid performance radar map, using 4 models trained on *Baseline* (green) and *Joint-train* (blue) paradigms in underrepresented high-risk sets.

### D. Classification Robustness in Out-domain Conditions

We further explored the impact of synthetic samples from *Ctrl-GenAug* on diagnostic robustness in out-domain settings using the carotid dataset. Training data of the sequence generator consisted of labeled ID and unlabeled OD subsets. We added the hospital identifier in the descriptive text of the ID data to condition the domain distribution. For the OD data, which did not contain the diagnostic class label, we padded the corresponding conditioning vector with zeros, while solely preserving hospital IDs to form descriptive texts. As shown in Table III, the average accuracy and AUROC of three classifiers display better results on the *Real-finetune* and *Joint-train* paradigms compared to the *Baseline*. It validates that diagnostic robustness can be enhanced with the aid of *Ctrl-GenAug* in scenarios where we only have access to unlabeled cases from additional medical centers due to limited resources.

TABLE III

OUT-DOMAIN PERFORMANCE COMPARISON USING THREE NETS TRAINED ON *Baseline* (A), *Real-finetune* (B), AND *Joint-train* (C) PARADIGMS IN CAROTID DATASET. "HYBRID", THE NET WITH CNN-TRANSFORMER DESIGN. ACC., ACCURACY (%).

Method	Backbone	Training Paradigm	Carotid			
			Acc.	$\Delta$	AUROC	$\Delta$
I3D [79]	CNN	A	70.00		0.609	
		B	71.67	$\uparrow 1.67$	0.648	$\uparrow 0.039$
		C	75.00	$\uparrow 5.00$	0.682	$\uparrow 0.073$
TPN [83]	CNN	A	75.00		0.667	
		B	76.67	$\uparrow 1.67$	0.731	$\uparrow 0.064$
		C	76.67	$\uparrow 1.67$	0.678	$\uparrow 0.011$
CSG-3DCT [1]	Hybrid	A	68.33		0.599	
		B	73.33	$\uparrow 5.00$	0.689	$\uparrow 0.090$
		C	70.00	$\uparrow 1.67$	0.651	$\uparrow 0.052$

### E. Analysis of Multimodal Conditions Guidance

To illustrate the role of different conditional guidance, we conduct comparative experiments with generators that resort to various banks of conditions for training and sampling. Table IV validates that all proposed conditions are effective for enhancing synthesis and diagnosis tasks. Specifically, without text control, the downstream diagnostic performance is comparatively poor. Fig. 5(b-c) compares typical synthetic thyroid nodule sequences generated under condition banks with and without text guidance. The former is visibly high-fidelity and faithful to the given text prompt (e.g., smooth margin), while the latter exhibits less distinguishable features for diagnosis (e.g., blurry margin). That is to say, the proposed *Ctrl-GenAug* can create more diagnosis-reliable samples by enhancing semantic steerability in the generation process. Besides, by incorporating image prior knowledge in the sampling process, the average accuracy and AUROC of three classifiers are improved by 4.20% and 0.040, respectively. This proves the domain gap between synthetic and real samples is mitigated by introducing the image prior. Moreover, as shown in Table IV, conditioning the generator on the motion field produces more content-consistent and smoother samples, leading to continuous improvements in diagnostic performance. It can also be

observed that the FVD results show a limited correlation with downstream evaluation metrics, confirming the finding in [7].

### F. Impact of the Sequential Augmentation Module

To verify the impact of the proposed sequential augmentation module, as shown in Table V, we compared the performance of three generator variants on the synthesis and downstream tasks. Ours-S, Ours-SK, and Ours-SKM denote our ablation studies, including gradually adding sequential attention ('-S'), key-frame/slice attention ('-K'), and motion field attention ('-M') to the generator with spatial inflation only. Table V shows that the downstream accuracy and AUROC improvements of Ours-SKM are significantly higher than those of Ours-S and Ours-SK in both datasets. In terms of quantitative assessment of sequential coherence, Ours-SKM achieves better results overall than other variants. These prove that this module can help the generator synthesize cross-frame/slice consistent and dynamic-smooth clips, which are diagnosis-promotive for downstream diagnostic tasks. Moreover, it can be observed that the FVD results across these three generators show no significant difference, revealing its limited value for evaluating diagnosis-oriented medical sequence synthesis tasks.

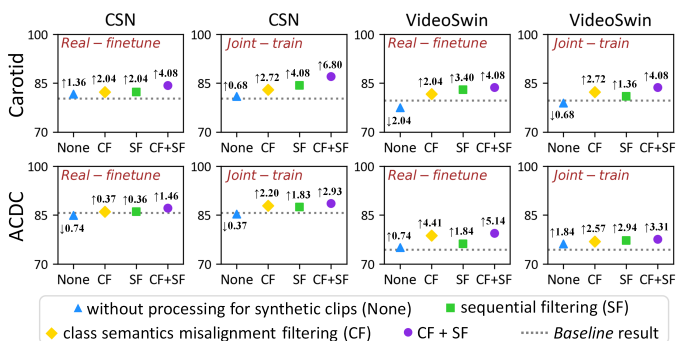


Fig. 7. Carotid stenosis and heart disease diagnostic accuracy (%) comparison using two classifiers on our filtering strategies under *Real-finetune* and *Joint-train* paradigms. The accuracy gains over the *Baseline* are depicted.

### G. Effectiveness of the Noisy Synthetic Data Filter

As shown in Fig. 7, we validated the indispensable role of our proposed noisy synthetic data filter by assessing its impact on downstream diagnostic accuracy, using two classifiers trained on *Real-finetune* and *Joint-train* paradigms across the carotid and ACDC datasets. For instance, on the carotid dataset, the *Joint-train* CSN resorting to non-quality controlled synthetic clips (i.e., 'None'), displays no significant difference with its *Baseline* (80.95% vs. 80.27%), even an accuracy degradation for its VideoSwin counterpart (78.91% vs. 79.59%). Then, by implementing our CF and SF strategy, diagnostic accuracy is significantly improved by 2.04% and 3.40%, respectively. Equipped with both, it achieves an accuracy of 87.07%, outperforming the 'None' by 6.12%.

### H. Impacts of Traditional and Generative Augmentations

We tested the contributions of different data augmentations in three downstream diagnostic tasks. The traditional augmentations used in this experiment can be found in Table I. We

TABLE IV

ABLATION STUDY FOR DIFFERENT CONDITIONAL CONTROLS IN TUSC [69], INCLUDING CLASS LABEL (C), TEXT (T), IMAGE PRIOR (I), AND MOTION FIELD (MF). SLOWFAST [81] (C1), CSN [82] (C2), AND FTC [78] (C3) TRAINED ON *Joint-train* PARADIGM WERE USED FOR DOWNSTREAM DIAGNOSIS. "HYBRID", THE CLASSIFIER WITH CNN-TRANSFORMER DESIGN.

Dataset	Synthesis						Downstream Diagnosis			
	Control				Metric		Backbone	$\Delta$ Accuracy	$\Delta$ AUROC	
	C	T	I	MF	FVD $\downarrow$	VAE-Seq $\uparrow$				Dynamic Smoothness $\uparrow$
TUSC [69]	✓		✓	✓	4.18	90.40%	95.03%	C1 CNN $\downarrow$ 1.80%	$\downarrow$ 0.015	
								C2 CNN $\uparrow$ 1.44%	$\uparrow$ 0.022	
								C3 Hybrid $\uparrow$ 1.08%	$\uparrow$ 0.030	
	✓	✓		✓	7.01	90.51%	<b>96.91%</b>	C1 CNN $\downarrow$ 1.08%	$\downarrow$ 0.001	
							C2 CNN $\downarrow$ 0.36%	$\downarrow$ 0.008		
							C3 Hybrid $\downarrow$ 1.44%	$\downarrow$ 0.011		
	✓	✓	✓		5.59	91.56%	94.66%	C1 CNN $\uparrow$ 1.80%	$\uparrow$ 0.017	
								C2 CNN $\uparrow$ 1.08%	$\uparrow$ 0.014	
								C3 Hybrid $\uparrow$ 2.16%	$\uparrow$ 0.016	
	✓	✓	✓	✓	<b>3.69</b>	<b>92.14%</b>	95.59%	C1 CNN $\uparrow$ 2.53%	$\uparrow$ 0.030	
								C2 CNN $\uparrow$ 3.61%	$\uparrow$ 0.040	
								C3 Hybrid $\uparrow$ 3.57%	$\uparrow$ 0.030	

TABLE V

ABLATION STUDY FOR THE SEQUENTIAL AUGMENTATION MODULE OF THE GENERATOR IN TUSC [69] AND ACDC [70]. SLOWFAST [81] (C1), CSN [82] (C2), AND FTC [78] (C3) TRAINED ON *Joint-train* PARADIGM WERE USED FOR DOWNSTREAM DIAGNOSIS. "HYBRID", THE CLASSIFIER WITH CNN-TRANSFORMER DESIGN.

Dataset	Synthesis				Downstream Diagnosis			
	FVD $\downarrow$	VAE-Seq $\uparrow$	Dynamic Smoothness $\uparrow$		Backbone	$\Delta$ Accuracy	$\Delta$ AUROC	
Ours-S					C1 CNN $\downarrow$ 0.36%	$\downarrow$ 0.009		
					C2 CNN $\uparrow$ 1.08%	$\uparrow$ 0.011		
					C3 Hybrid $\uparrow$ 1.44%	$\uparrow$ 0.007		
TUSC [69]					C1 CNN $\uparrow$ 0.72%	$\uparrow$ 0.007		
					C2 CNN $\uparrow$ 2.88%	$\uparrow$ 0.032		
					C3 Hybrid $\uparrow$ 3.24%	$\uparrow$ 0.021		
Ours-SKM	<b>3.69</b>	<b>92.14%</b>	<b>95.59%</b>		C1 CNN $\uparrow$ 2.53%	$\uparrow$ 0.030		
					C2 CNN $\uparrow$ 3.61%	$\uparrow$ 0.040		
					C3 Hybrid $\uparrow$ 3.57%	$\uparrow$ 0.030		
Ours-S					C1 CNN $\uparrow$ 0.73%	$\uparrow$ 0.015		
					C2 CNN $\downarrow$ 0.37%	$\uparrow$ 0.000		
					C3 Hybrid $\downarrow$ 0.73%	$\downarrow$ 0.005		
ACDC [70]					C1 CNN $\uparrow$ 1.47%	$\uparrow$ 0.021		
					C2 CNN $\uparrow$ 1.83%	$\uparrow$ 0.032		
					C3 Hybrid $\uparrow$ 1.83%	$\uparrow$ 0.014		
Ours-SKM	<b>8.18</b>	77.08%	<b>92.77%</b>		C1 CNN $\uparrow$ 2.20%	$\uparrow$ 0.040		
					C2 CNN $\uparrow$ 2.93%	$\uparrow$ 0.049		
					C3 Hybrid $\uparrow$ 3.43%	$\uparrow$ 0.029		

TABLE VI

ABLATION STUDY FOR AUGMENTATION-FREE (NONE), TRADITIONAL AUGMENTATION (TRAUG), AND GENERATIVE AUGMENTATION (GENAUG) USING I3D [79] IN THREE DIAGNOSTIC TASKS. FOR GENAUG, BOTH *Real-finetune* AND *Joint-train* PARADIGMS WERE INVESTIGATED. ACC., ACCURACY (%).

Generative Training Paradigm	Augmentation Method	Carotid				TUSC [69]				ACDC [70]			
		Acc.	$\Delta$	AUROC	$\Delta$	Acc.	$\Delta$	AUROC	$\Delta$	Acc.	$\Delta$	AUROC	$\Delta$
/	None	75.51		0.718		59.28		0.532		80.55		0.681	
/	TraAug	79.59	$\uparrow$ 4.08	0.737	$\uparrow$ 0.019	60.72	$\uparrow$ 1.44	0.559	$\uparrow$ 0.027	83.49	$\uparrow$ 2.94	0.733	$\uparrow$ 0.052
Real-finetune	TraAug + GenAug	<b>85.03</b>	$\uparrow$ 9.52	<b>0.813</b>	$\uparrow$ 0.095	<b>65.41</b>	$\uparrow$ 6.13	<b>0.611</b>	$\uparrow$ 0.079	<b>87.16</b>	$\uparrow$ 6.61	<b>0.795</b>	$\uparrow$ 0.114
/	None	78.91		0.735		60.36		0.552		80.92		0.688	
/	TraAug	80.95	$\uparrow$ 2.04	0.751	$\uparrow$ 0.016	61.08	$\uparrow$ 0.72	0.562	$\uparrow$ 0.010	81.28	$\uparrow$ 0.36	0.696	$\uparrow$ 0.008
Joint-train	TraAug + GenAug	<b>84.35</b>	$\uparrow$ 5.44	<b>0.811</b>	$\uparrow$ 0.076	<b>62.88</b>	$\uparrow$ 2.52	<b>0.578</b>	$\uparrow$ 0.026	<b>85.32</b>	$\uparrow$ 4.40	<b>0.762</b>	$\uparrow$ 0.074

report the performance gains of the two variants with data augmentations compared to the augmentation-free setup. For experimental fairness, we kept the training datasets for the None and TraAug variants the same size as the method combining traditional and generative augmentations. As presented

in Table VI, the diagnostic performance shows noticeable improvements using the traditional augmentation method. Further coupled with the generative augmentation, the results show more substantial improvements than TraAug. We also observe that in the case of using traditional augmentation, adding extra

real training samples yields limited performance gains, even a drop for ACDC. These prove that generative augmentation can effectively supplement traditional data augmentation and provide intrinsically diverse data characteristics for enhancing deep classifier learning, which support the viewpoints of [7].

## V. CONCLUSION AND DISCUSSION

In this study, we present a new and general diffusion-based generative augmentation framework, named *Ctrl-GenAug*, to facilitate medical sequence classification by leveraging customized and diagnosis-reliable synthetic sequences. To the best of our knowledge, this is the first comprehensive study to investigate the impact of the controllable generative augmentation scheme on aiding medical sequence classification. To improve the quality of synthetic data for promoting downstream classification, we propose a multimodal conditions-guided medical sequence generator that ensures flexibly controllable synthesis across semantic, sequential, and data distribution aspects. Moreover, we propose a highly effective noisy synthetic data filter to better learn from synthetic data, including adaptively filtering diagnosis-inhibitive synthetic sequences at class semantics and sequential levels. This can better connect the synthesis task and the downstream one, thus further enhancing our sequence classification performance. Extensive experiments on 3 medical datasets across multiple organs and modalities, with 11 popular networks trained on 3 paradigms, show the effectiveness and generality of *Ctrl-GenAug*. Furthermore, we conduct extensive empirical analysis demonstrating that *Ctrl-GenAug* can be effectively leveraged to improve diagnostic performance in underrepresented high-risk populations and out-domain robustness. We believe that *Ctrl-GenAug* can serve as a robust and practical data augmentation tool for various clinical scenarios.

We then discuss the limitations of *Ctrl-GenAug*. First, the denoising diffusion implicit model (DDIM) sampling process is time-consuming due to the large inference steps. This limits the clinical practicality of *Ctrl-GenAug* for fast and large-scale production. Second, in out-domain conditions, the proposed framework requires target domain data during generator training, which can be tough to obtain in advance in clinical practice. In future work, we will adopt fast-sampling strategies (e.g., AMED-Solver [88]) to better balance the trade-off between sampling time and sample quality. Besides, we will incorporate test-time adaptation methods [89], [90] to provide a more user-friendly tool for out-domain applications in clinical settings. Last, we will attempt to further extend the proposed method to segmentation and detection tasks.

## REFERENCES

- [1] X. Zhou, Y. Huang, W. Xue, X. Yang, Y. Zou, Q. Ying, Y. Zhang, J. Liu, J. Ren, and D. Ni, "Inflated 3d convolution-transformer for weakly-supervised carotid stenosis grading with ultrasound videos," in *International Conference on Medical Image Computing and Computer-Assisted Intervention*. Springer, 2023, pp. 511–520.
- [2] Y.-R. Wang, K. Yang, Y. Wen, P. Wang, Y. Hu, Y. Lai, Y. Wang, K. Zhao, S. Tang, A. Zhang *et al.*, "Screening and diagnosis of cardiovascular disease using artificial intelligence-enabled cardiac magnetic resonance imaging," *Nature Medicine*, pp. 1–10, 2024.
- [3] G. Varoquaux and V. Cheplygina, "Machine learning for medical imaging: methodological failures and recommendations for the future," *NPJ digital medicine*, vol. 5, no. 1, p. 48, 2022.
- [4] Y. Huang, X. Yang, X. Huang, J. Liang, X. Zhou, C. Chen, H. Dou, X. Hu, Y. Cao, and D. Ni, "Online reflective learning for robust medical image segmentation," in *International Conference on Medical Image Computing and Computer-Assisted Intervention*. Springer, 2022, pp. 652–662.
- [5] F.-A. Croitoru, V. Hondru, R. T. Ionescu, and M. Shah, "Diffusion models in vision: A survey," *IEEE Transactions on Pattern Analysis and Machine Intelligence*, vol. 45, no. 9, pp. 10 850–10 869, 2023.
- [6] P. Dhariwal and A. Nichol, "Diffusion models beat gans on image synthesis," *Advances in neural information processing systems*, vol. 34, pp. 8780–8794, 2021.
- [7] Y. Luo, Q. Yang, Y. Fan, H. Qi, and M. Xia, "Measurement guidance in diffusion models: Insight from medical image synthesis," *IEEE Transactions on Pattern Analysis and Machine Intelligence*, 2024.
- [8] R. Rombach, A. Blattmann, D. Lorenz, P. Esser, and B. Ommer, "High-resolution image synthesis with latent diffusion models," in *Proceedings of the IEEE/CVF conference on computer vision and pattern recognition*, 2022, pp. 10 684–10 695.
- [9] F. Zhan, Y. Yu, R. Wu, J. Zhang, S. Lu, L. Liu, A. Kortylewski, C. Theobalt, and E. Xing, "Multimodal image synthesis and editing: The generative ai era," *IEEE Transactions on Pattern Analysis and Machine Intelligence*, vol. 45, no. 12, pp. 15 098–15 119, 2023.
- [10] U. Singer, A. Polyak, T. Hayes, X. Yin, J. An, S. Zhang, Q. Hu, H. Yang, O. Ashual, O. Gafni *et al.*, "Make-a-video: Text-to-video generation without text-video data," *arXiv preprint arXiv:2209.14792*, 2022.
- [11] D. Zhou, W. Wang, H. Yan, W. Lv, Y. Zhu, and J. Feng, "Magicvideo: Efficient video generation with latent diffusion models," *arXiv preprint arXiv:2211.11018*, 2022.
- [12] S. Ge, S. Nah, G. Liu, T. Poon, A. Tao, B. Catanzaro, D. Jacobs, J.-B. Huang, M.-Y. Liu, and Y. Balaji, "Preserve your own correlation: A noise prior for video diffusion models," in *Proceedings of the IEEE/CVF International Conference on Computer Vision*, 2023, pp. 22 930–22 941.
- [13] J. Ho, T. Salimans, A. Gritsenko, W. Chan, M. Norouzi, and D. J. Fleet, "Video diffusion models," *arXiv preprint arXiv:2204.03458*, 2022.
- [14] R. Wu, L. Chen, T. Yang, C. Guo, C. Li, and X. Zhang, "Lamp: Learn a motion pattern for few-shot-based video generation," *arXiv preprint arXiv:2310.10769*, 2023.
- [15] J. Wang, Y. Zhang, J. Zou, Y. Zeng, G. Wei, L. Yuan, and H. Li, "Boximator: Generating rich and controllable motions for video synthesis," *arXiv preprint arXiv:2402.01566*, 2024.
- [16] W. Ren, H. Yang, G. Zhang, C. Wei, X. Du, W. Huang, and W. Chen, "Consisti2v: Enhancing visual consistency for image-to-video generation," *Transactions on Machine Learning Research*, 2024.
- [17] J. Han, F. Kokkinos, and P. Torr, "Vfusion3d: Learning scalable 3d generative models from video diffusion models," *arXiv preprint arXiv:2403.12034*, 2024.
- [18] L. Khachatryan, A. Movsisyan, V. Tadevosyan, R. Henschel, Z. Wang, S. Navasardyan, and H. Shi, "Text2video-zero: Text-to-image diffusion models are zero-shot video generators," in *Proceedings of the IEEE/CVF International Conference on Computer Vision*, 2023, pp. 15 954–15 964.
- [19] Y. Zhang, Y. Wei, D. Jiang, X. Zhang, W. Zuo, and Q. Tian, "Controlvideo: Training-free controllable text-to-video generation," *arXiv preprint arXiv:2305.13077*, 2023.
- [20] C. Qi, X. Cun, Y. Zhang, C. Lei, X. Wang, Y. Shan, and Q. Chen, "Fatezero: Fusing attentions for zero-shot text-based video editing," in *Proceedings of the IEEE/CVF International Conference on Computer Vision*, 2023, pp. 15 932–15 942.
- [21] X. Guo, M. Zheng, L. Hou, Y. Gao, Y. Deng, P. Wan, D. Zhang, Y. Liu, W. Hu, Z. Zha *et al.*, "I2v-adapter: A general image-to-video adapter for diffusion models," in *ACM SIGGRAPH 2024 Conference Papers*, 2024, pp. 1–12.
- [22] L. Uzolas, E. Eisemann, and P. Kellnhofer, "Motiondreamer: Zero-shot 3d mesh animation from video diffusion models," *arXiv preprint arXiv:2405.20155*, 2024.
- [23] X. Zhou, Y. Huang, W. Xue, H. Dou, J. Cheng, H. Zhou, and D. Ni, "Heartbeat: Towards controllable echocardiography video synthesis with multimodal conditions-guided diffusion models," *arXiv preprint arXiv:2406.14098*, 2024.
- [24] C. Li, H. Liu, Y. Liu, B. Y. Feng, W. Li, X. Liu, Z. Chen, J. Shao, and Y. Yuan, "Endora: Video generation models as endoscopy simulators," *arXiv preprint arXiv:2403.11050*, 2024.

- [25] I. Ktena, O. Wiles, I. Albuquerque, S.-A. Rebuffi, R. Tanno, A. G. Roy, S. Azizi, D. Belgrave, P. Kohli, T. Cemgil *et al.*, “Generative models improve fairness of medical classifiers under distribution shifts,” *Nature Medicine*, pp. 1–8, 2024.
- [26] R. He, S. Sun, X. Yu, C. Xue, W. Zhang, P. Torr, S. Bai, and X. Qi, “IS SYNTHETIC DATA FROM GENERATIVE MODELS READY FOR IMAGE RECOGNITION?” in *The Eleventh International Conference on Learning Representations*, 2023.
- [27] J. Zhu, Y. Qi, and J. Wu, “Medical sam 2: Segment medical images as video via segment anything model 2,” *arXiv preprint arXiv:2408.00874*, 2024.
- [28] A. Blattmann, R. Rombach, H. Ling, T. Dockhorn, S. W. Kim, S. Fidler, and K. Kreis, “Align your latents: High-resolution video synthesis with latent diffusion models,” in *Proceedings of the IEEE/CVF Conference on Computer Vision and Pattern Recognition*, 2023, pp. 22 563–22 575.
- [29] J. Ho, W. Chan, C. Saharia, J. Whang, R. Gao, A. Gritsenko, D. P. Kingma, B. Poole, M. Norouzi, D. J. Fleet *et al.*, “Imagen video: High definition video generation with diffusion models,” *arXiv preprint arXiv:2210.02303*, 2022.
- [30] Y. Guo, C. Yang, A. Rao, Y. Wang, Y. Qiao, D. Lin, and B. Dai, “Animatediff: Animate your personalized text-to-image diffusion models without specific tuning,” *arXiv preprint arXiv:2307.04725*, 2023.
- [31] D. J. Zhang, D. Li, H. Le, M. Z. Shou, C. Xiong, and D. Sahoo, “Moonshot: Towards controllable video generation and editing with multimodal conditions,” *arXiv preprint arXiv:2401.01827*, 2024.
- [32] M. Zhao, R. Wang, F. Bao, C. Li, and J. Zhu, “Controlvideo: Conditional control for one-shot text-driven video editing and beyond,” *arXiv preprint arXiv:2305.17098*, 2023.
- [33] X. Wang, H. Yuan, S. Zhang, D. Chen, J. Wang, Y. Zhang, Y. Shen, D. Zhao, and J. Zhou, “Videocomposer: Compositional video synthesis with motion controllability,” *Advances in Neural Information Processing Systems*, vol. 36, 2024.
- [34] C. Zach, T. Pock, and H. Bischof, “A duality based approach for realtime tv-l 1 optical flow,” in *Pattern Recognition: 29th DAGM Symposium, Heidelberg, Germany, September 12-14, 2007. Proceedings 29*. Springer, 2007, pp. 214–223.
- [35] F. Liang, B. Wu, J. Wang, L. Yu, K. Li, Y. Zhao, I. Misra, J.-B. Huang, P. Zhang, P. Vajda *et al.*, “Flowvid: Taming imperfect optical flows for consistent video-to-video synthesis,” *arXiv preprint arXiv:2312.17681*, 2023.
- [36] H. Ni, C. Shi, K. Li, S. X. Huang, and M. R. Min, “Conditional image-to-video generation with latent flow diffusion models,” in *Proceedings of the IEEE/CVF Conference on Computer Vision and Pattern Recognition*, 2023, pp. 18 444–18 455.
- [37] H. Reynaud, M. Qiao, M. Dombrowski, T. Day, R. Razavi, A. Gomez, P. Leeson, and B. Kainz, “Feature-conditioned cascaded video diffusion models for precise echocardiogram synthesis,” in *International Conference on Medical Image Computing and Computer-Assisted Intervention*. Springer, 2023, pp. 142–152.
- [38] N. Van Phi, T. M. Duc, P. H. Hieu, and T. Q. Long, “Echocardiography video synthesis from end diastolic semantic map via diffusion model,” in *ICASSP 2024-2024 IEEE International Conference on Acoustics, Speech and Signal Processing (ICASSP)*. IEEE, 2024, pp. 13 461–13 465.
- [39] V. P. Nguyen, T. N. L. Ha, H. H. Pham, and Q. L. Tran, “Training-free condition video diffusion models for single frame spatial-semantic echocardiogram synthesis,” *arXiv preprint arXiv:2408.03035*, 2024.
- [40] Y. Wang, J. Zhang, and Y. Wang, “Do generated data always help contrastive learning?” in *The Twelfth International Conference on Learning Representations*, 2024.
- [41] M. B. Sarryıldız, K. Alahari, D. Larlus, and Y. Kalantidis, “Fake it till you make it: Learning transferable representations from synthetic imagenet clones,” in *Proceedings of the IEEE/CVF Conference on Computer Vision and Pattern Recognition (CVPR)*, June 2023, pp. 8011–8021.
- [42] B. Trabucco, K. Doherty, M. Gurinas, and R. Salakhutdinov, “Effective data augmentation with diffusion models,” *arXiv preprint arXiv:2302.07944*, 2023.
- [43] S. Azizi, S. Kornblith, C. Saharia, M. Norouzi, and D. J. Fleet, “Synthetic data from diffusion models improves imagenet classification,” *arXiv preprint arXiv:2304.08466*, 2023.
- [44] S. Sankaranarayanan, Y. Balaji, A. Jain, S. N. Lim, and R. Chellappa, “Learning from synthetic data: Addressing domain shift for semantic segmentation,” in *Proceedings of the IEEE conference on computer vision and pattern recognition*, 2018, pp. 3752–3761.
- [45] W. Wu, Y. Zhao, M. Z. Shou, H. Zhou, and C. Shen, “Diffmask: Synthesizing images with pixel-level annotations for semantic segmentation using diffusion models,” in *Proceedings of the IEEE/CVF International Conference on Computer Vision*, 2023, pp. 1206–1217.
- [46] L. Yang, X. Xu, B. Kang, Y. Shi, and H. Zhao, “Freemask: Synthetic images with dense annotations make stronger segmentation models,” *Advances in Neural Information Processing Systems*, vol. 36, 2024.
- [47] C. Feng, Y. Zhong, Z. Jie, W. Xie, and L. Ma, “Instagen: Enhancing object detection by training on synthetic dataset,” in *Proceedings of the IEEE/CVF Conference on Computer Vision and Pattern Recognition*, 2024, pp. 14 121–14 130.
- [48] K. Singh, T. Navaratnam, J. Holmer, S. Schaub-Meyer, and S. Roth, “Is synthetic data all we need? benchmarking the robustness of models trained with synthetic images,” in *Proceedings of the IEEE/CVF Conference on Computer Vision and Pattern Recognition*, 2024, pp. 2505–2515.
- [49] F. Shang, J. Fu, Y. Yang, H. Huang, J. Liu, and L. Ma, “Synfundus: A synthetic fundus images dataset with millions of samples and multi-disease annotations,” *arXiv preprint arXiv:2312.00377*, 2023.
- [50] M. A. Farooq, W. Yao, M. Schukat, M. A. Little, and P. Corcoran, “Derm-t2im: Harnessing synthetic skin lesion data via stable diffusion models for enhanced skin disease classification using vit and cnn,” *arXiv preprint arXiv:2401.05159*, 2024.
- [51] Z. Zhang, L. Yao, B. Wang, D. Jha, E. Keles, A. Medetalibeyoglu, and U. Bagci, “Emit-diff: Enhancing medical image segmentation via text-guided diffusion model,” *arXiv preprint arXiv:2310.12868*, 2023.
- [52] Z. Dorjsembe, H.-K. Pao, and F. Xiao, “Polyp-ddpm: Diffusion-based semantic polyp synthesis for enhanced segmentation,” *arXiv preprint arXiv:2402.04031*, 2024.
- [53] W. Li, H. Xu, G. Zhang, H.-a. Gao, M. Gao, M. Wang, and H. Zhao, “Fairdiff: Fair segmentation with point-image diffusion,” *arXiv preprint arXiv:2407.06250*, 2024.
- [54] J. Sohl-Dickstein, E. Weiss, N. Maheswaranathan, and S. Ganguli, “Deep unsupervised learning using nonequilibrium thermodynamics,” in *International conference on machine learning*. PMLR, 2015, pp. 2256–2265.
- [55] J. Ho, A. Jain, and P. Abbeel, “Denoising diffusion probabilistic models,” *Advances in neural information processing systems*, vol. 33, pp. 6840–6851, 2020.
- [56] P. Esser, R. Rombach, and B. Ommer, “Taming transformers for high-resolution image synthesis,” in *Proceedings of the IEEE/CVF conference on computer vision and pattern recognition*, 2021, pp. 12 873–12 883.
- [57] O. Ronneberger, P. Fischer, and T. Brox, “U-net: Convolutional networks for biomedical image segmentation,” in *Medical Image Computing and Computer-Assisted Intervention—MICCAI 2015: 18th International Conference, Munich, Germany, October 5-9, 2015, Proceedings, Part III 18*. Springer, 2015, pp. 234–241.
- [58] Y. Huang, X. Yang, L. Liu, H. Zhou, A. Chang, X. Zhou, R. Chen, J. Yu, J. Chen, C. Chen *et al.*, “Segment anything model for medical images?” *Medical Image Analysis*, vol. 92, p. 103061, 2024.
- [59] A. Radford *et al.*, “Learning transferable visual models from natural language supervision,” in *International conference on machine learning*. PMLR, 2021, pp. 8748–8763.
- [60] H. Ye, J. Zhang, S. Liu, X. Han, and W. Yang, “Ip-adapter: Text compatible image prompt adapter for text-to-image diffusion models,” *arXiv preprint arXiv:2308.06721*, 2023.
- [61] L. Bommers, X. Lin, and J. Zhou, “Mvmed: Fast multi-object tracking in the compressed domain,” in *2020 15th IEEE Conference on Industrial Electronics and Applications (ICIEA)*, 2020, pp. 1419–1424.
- [62] Y. Cong, M. Xu, christian simon, S. Chen, J. Ren, Y. Xie, J.-M. Perez-Rua, B. Rosenhahn, T. Xiang, and S. He, “FLATTEN: optical FLOW-guided ATTENTION for consistent text-to-video editing,” in *The Twelfth International Conference on Learning Representations*, 2024.
- [63] G. Kwon, M. Prabhushankar, D. Temel, and G. AlRegib, “Backpropagated gradient representations for anomaly detection,” in *Computer Vision—ECCV 2020: 16th European Conference, Glasgow, UK, August 23–28, 2020, Proceedings, Part XXI 16*. Springer, 2020, pp. 206–226.
- [64] J. Macqueen, *Some methods for classification and analysis of multivariate observations*. University of California Press, 1967.
- [65] M. Heusel, H. Ramsauer, T. Unterthiner, B. Nessler, and S. Hochreiter, “Gans trained by a two time-scale update rule converge to a local nash equilibrium,” *Advances in neural information processing systems*, vol. 30, 2017.
- [66] T. Unterthiner, S. Van Steenkiste, K. Kurach, R. Marinier, M. Michalski, and S. Gelly, “Towards accurate generative models of video: A new metric & challenges,” *arXiv preprint arXiv:1812.01717*, 2018.
- [67] Z. Huang, Y. He, J. Yu, F. Zhang, C. Si, Y. Jiang, Y. Zhang, T. Wu, Q. Jin, N. Chanpaisit *et al.*, “Vbench: Comprehensive benchmark

- suite for video generative models,” in *Proceedings of the IEEE/CVF Conference on Computer Vision and Pattern Recognition*, 2024, pp. 21 807–21 818.
- [68] Z. Li, Z.-L. Zhu, L.-H. Han, Q. Hou, C.-L. Guo, and M.-M. Cheng, “Amt: All-pairs multi-field transforms for efficient frame interpolation,” in *Proceedings of the IEEE/CVF Conference on Computer Vision and Pattern Recognition*, 2023, pp. 9801–9810.
- [69] Stanford-AIMI, “Thyroid ultrasound cine-clip,” <https://stanfordaimi.azurewebsites.net/datasets/a72f2b02-7b53-4c5d-963c-d7253220bfd5/>, 2021.
- [70] O. Bernard, A. Lalonde, C. Zotti, F. Cervenansky, X. Yang, P.-A. Heng, I. Cetin, K. Lekadir, O. Camara, M. A. G. Ballester *et al.*, “Deep learning techniques for automatic mri cardiac multi-structures segmentation and diagnosis: is the problem solved?” *IEEE transactions on medical imaging*, vol. 37, no. 11, pp. 2514–2525, 2018.
- [71] J. Ho and T. Salimans, “Classifier-free diffusion guidance,” *arXiv preprint arXiv:2207.12598*, 2022.
- [72] J. Liang, X. Yang, Y. Huang, H. Li, S. He, X. Hu, Z. Chen, W. Xue, X. Yang, and D. Ni, “Sketch guided and progressive growing gan for realistic and editable ultrasound image synthesis,” *Medical image analysis*, vol. 79, p. 102461, 2022.
- [73] J. Liu, X. Zhou, H. Lin, X. Lu, J. Zheng, E. Xu, D. Jiang, H. Zhang, X. Yang, J. Zhong *et al.*, “Deep learning based on carotid transverse b-mode scan videos for the diagnosis of carotid plaque: a prospective multicenter study,” *European Radiology*, vol. 33, no. 5, pp. 3478–3487, 2023.
- [74] F. N. Tessler, W. D. Middleton, E. G. Grant, J. K. Hoang, L. L. Berland, S. A. Teefey, J. J. Cronan, M. D. Beland, T. S. Desser, M. C. Frates, L. W. Hammers, U. M. Hamper, J. E. Langer, C. C. Reading, L. M. Scoutt, and A. T. Stavros, “Acr thyroid imaging, reporting and data system (ti-rads): White paper of the acr ti-rads committee,” *Journal of the American College of Radiology*, vol. 14, no. 5, pp. 587–595, 2017.
- [75] R. Yamashita, T. Kapoor, M. N. Alam, A. Galimzianova, S. A. Syed, M. Ugur Akdogan, E. Alkim, A. L. Wentland, N. Madhuripan, D. Goff *et al.*, “Toward reduction in false-positive thyroid nodule biopsies with a deep learning-based risk stratification system using us cine-clip images,” *Radiology: Artificial Intelligence*, vol. 4, no. 3, p. e210174, 2022.
- [76] L. Huang, D. Chen, Y. Liu, Y. Shen, D. Zhao, and J. Zhou, “Composer: Creative and controllable image synthesis with composable conditions,” *arXiv preprint arXiv:2302.09778*, 2023.
- [77] M. Contributors, “Openmmlab’s next generation video understanding toolbox and benchmark,” <https://github.com/open-mmlab/mmaaction2>, 2020.
- [78] N. Ahmadi, M. Tsang, A. Gu, T. Tsang, and P. Abolmaesumi, “Transformer-based spatio-temporal analysis for classification of aortic stenosis severity from echocardiography cine series,” *IEEE Transactions on Medical Imaging*, 2023.
- [79] J. Carreira and A. Zisserman, “Quo vadis, action recognition? a new model and the kinetics dataset,” in *proceedings of the IEEE Conference on Computer Vision and Pattern Recognition*, 2017, pp. 6299–6308.
- [80] D. Tran, H. Wang, L. Torresani, J. Ray, Y. LeCun, and M. Paluri, “A closer look at spatiotemporal convolutions for action recognition,” in *Proceedings of the IEEE conference on Computer Vision and Pattern Recognition*, 2018, pp. 6450–6459.
- [81] C. Feichtenhofer, H. Fan, J. Malik, and K. He, “Slowfast networks for video recognition,” in *Proceedings of the IEEE/CVF international conference on computer vision*, 2019, pp. 6202–6211.
- [82] D. Tran, H. Wang, L. Torresani, and M. Feiszli, “Video classification with channel-separated convolutional networks,” in *Proceedings of the IEEE/CVF international conference on computer vision*, 2019, pp. 5552–5561.
- [83] C. Yang, Y. Xu, J. Shi, B. Dai, and B. Zhou, “Temporal pyramid network for action recognition,” in *Proceedings of the IEEE/CVF conference on computer vision and pattern recognition*, 2020, pp. 591–600.
- [84] G. Bertasius, H. Wang, and L. Torresani, “Is space-time attention all you need for video understanding?” in *ICML*, vol. 2, no. 3, 2021, p. 4.
- [85] Y. Li, C.-Y. Wu, H. Fan, K. Mangalam, B. Xiong, J. Malik, and C. Feichtenhofer, “Mvitv2: Improved multiscale vision transformers for classification and detection,” in *Proceedings of the IEEE/CVF Conference on Computer Vision and Pattern Recognition*, 2022, pp. 4804–4814.
- [86] Z. Liu, J. Ning, Y. Cao, Y. Wei, Z. Zhang, S. Lin, and H. Hu, “Video swin transformer,” in *Proceedings of the IEEE/CVF conference on computer vision and pattern recognition*, 2022, pp. 3202–3211.
- [87] K. Li, Y. Wang, Y. He, Y. Li, Y. Wang, L. Wang, and Y. Qiao, “Uniformerv2: Spatiotemporal learning by arming image vits with video uniformer,” *arXiv preprint arXiv:2211.09552*, 2022.
- [88] Z. Zhou, D. Chen, C. Wang, and C. Chen, “Fast ode-based sampling for diffusion models in around 5 steps,” in *Proceedings of the IEEE/CVF Conference on Computer Vision and Pattern Recognition*, 2024, pp. 7777–7786.
- [89] Y. Huang, X. Yang, X. Huang, X. Zhou, H. Chi, H. Dou, X. Hu, J. Wang, X. Deng, and D. Ni, “Fourier test-time adaptation with multi-level consistency for robust classification,” in *International Conference on Medical Image Computing and Computer-Assisted Intervention*. Springer, 2023, pp. 221–231.
- [90] L. Zhang, J. Nie, W. Wei, and Y. Zhang, “Unsupervised test-time adaptation learning for effective hyperspectral image super-resolution with unknown degeneration,” *IEEE Transactions on Pattern Analysis and Machine Intelligence*, 2024.
- [91] L. W. Sagers, J. A. Diao, L. Melas-Kyriazi, M. Groh, P. Rajpurkar, A. S. Adamson, V. Rotemberg, R. Daneshjou, and A. K. Manrai, “Augmenting medical image classifiers with synthetic data from latent diffusion models,” *arXiv preprint arXiv:2308.12453*, 2023.
- [92] B. Khosravi, F. Li, T. Dapamede, P. Rouzrokh, C. U. Gamble, H. M. Trivedi, C. C. Wyles, A. B. Sellegren, S. Purkayastha, B. J. Erickson *et al.*, “Synthetically enhanced: unveiling synthetic data’s potential in medical imaging research,” *EBioMedicine*, vol. 104, 2024.
- [93] H. Yu, Y. Li, N. Zhang, Z. Niu, X. Gong, Y. Luo, Q. Wu, W. Qin, M. Zhou, J. Han *et al.*, “Knowledge-driven ai-generated data for accurate and interpretable breast ultrasound diagnoses,” *arXiv preprint arXiv:2407.16634*, 2024.
- [94] H. Gong, Y. Wang, Y. Wang, J. Xiao, X. Wan, and H. Li, “Diffuse-uda: Addressing unsupervised domain adaptation in medical image segmentation with appearance and structure aligned diffusion models,” *arXiv preprint arXiv:2408.05985*, 2024.
- [95] L. Peng, Z. Zhang, G. Durak, F. H. Miller, A. Medetalibeyoglu, M. B. Wallace, and U. Bagci, “Optimizing synthetic data for enhanced pancreatic tumor segmentation,” *arXiv preprint arXiv:2407.19284*, 2024.
- [96] A. Kebaili, J. Lapuyade-Lahorgue, P. Vera, and S. Ruan, “3d mri synthesis with slice-based latent diffusion models: Improving tumor segmentation tasks in data-scarce regimes,” *arXiv preprint arXiv:2406.05421*, 2024.
- [97] Y. Yu, H. Chen, Z. Zhang, Q. Xiao, W. Lei, L. Dai, Y. Fu, H. Tan, G. Wang, P. Gao *et al.*, “Ct synthesis with conditional diffusion models for abdominal lymph node segmentation,” *arXiv preprint arXiv:2403.17770*, 2024.
- [98] Q. Chen, X. Chen, H. Song, Z. Xiong, A. Yuille, C. Wei, and Z. Zhou, “Towards generalizable tumor synthesis,” in *Proceedings of the IEEE/CVF Conference on Computer Vision and Pattern Recognition*, 2024, pp. 11 147–11 158.
- [99] Z. Dorjsembe, H.-K. Pao, S. Odonchimed, and F. Xiao, “Conditional diffusion models for semantic 3d brain mri synthesis,” *IEEE Journal of Biomedical and Health Informatics*, 2024.
- [100] K. Huang, X. Ma, Y. Zhang, N. Su, S. Yuan, Y. Liu, Q. Chen, and H. Fu, “Memory-efficient high-resolution oct volume synthesis with cascaded amortized latent diffusion models,” *arXiv preprint arXiv:2405.16516*, 2024.

## Supplementary Material

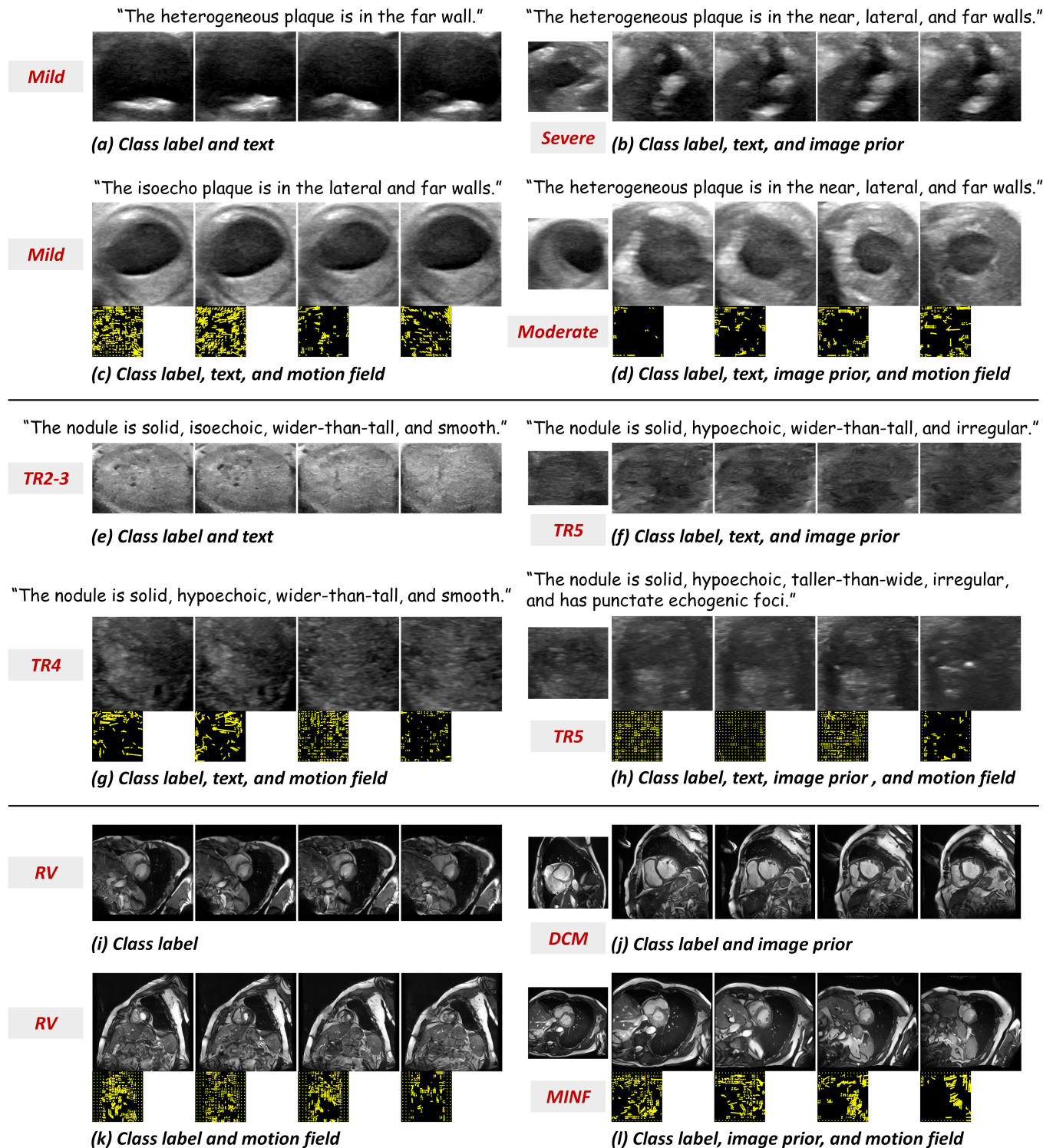


Fig. S1. Additional synthetic results on Carotid (a-d), TUSC [69] (e-h), and ACDC [70] (i-l). We used the multimodal conditions joint training strategy [76] during training and flexibly dropped several during sampling.



TABLE S1

A BRIEF REVIEW OF STUDIES IN THE MEDICAL FIELD UTILIZING DIFFUSION-BASED GENERATIVE MODELS TO PROMOTE DOWNSTREAM TASKS. WE CONSIDER SIX ASPECTS: THE CONDITIONAL CONTROL, THE DOWNSTREAM TASK, THE UNDERLYING ARCHITECTURE OF THE DOWNSTREAM NETWORK, THE NUMBER OF THE DOWNSTREAM NETWORK, AND THE MODALITY AND TYPE OF THE MEDICAL DATASET ON WHICH THE SURVEYED APPROACHES WERE APPLIED. ARCH., ARCHITECTURE. NUM., NUMBER. OCT, OPTICAL COHERENCE TOMOGRAPHY.

Study	Conditional Control	Downstream Task	Downstream Arch.	Downstream Net Num.	Medical Modality	Data Type
Shang et al. [49]	disease class, image readability	classification	CNN-based, Transformer-based	2	Fundus	image
Farooq et al. [50]	text	classification	CNN-based, Transformer-based	2	Dermoscopy	image
Zhang et al. [51]	text, edge	segmentation	CNN-Transformer hybrid-based	1	US, CT, MRI	image
Sagers et al. [91]	text	classification	CNN-based	1	Dermoscopy	image
Khosravi et al. [92]	attribute, 14 pathology labels	classification	CNN-based	1	X-ray	image
Yu et al. [93]	pathology labels, lesion bounding boxes, device types, pathology-specific knowledge (NCM/CAL labels)	classification	Transformer-based	1	US	image
Ktena et al. [25]	disease class, attribute	classification	CNN-based	1	Histopathology, X-ray, Dermoscopy	image
Luo et al. [7]	disease class	classification	CNN-based	10	Fundus, Dermoscopy, X-ray, US	image
Li et al. [24]	multi-scale latent representation	classification	Transformer-based	1	Endoscopy	video
Gong et al. [94]	mask	segmentation	CNN-based	1	MRI	volume
Peng et al. [95]	mask	segmentation	CNN-based, CNN-Transformer hybrid-based	3	CT	volume
Kebaili et al. [96]	tumor attribute, mask	segmentation	CNN-based	1	MRI	volume
Yu et al. [97]	mask	segmentation	CNN-based	1	CT	volume
Chen et al. [98]	mask	segmentation	CNN-based, CNN-Transformer hybrid-based	3	CT	volume
Dorjsembe et al. [99]	mask	segmentation	CNN-based	1	MRI	volume
Huang et al. [100]	mask	segmentation	CNN-based	2	OCT	volume
Ours	disease class, text, image prior, motion field	classification	CNN-based, Transformer-based, CNN-Transformer hybrid-based	11	US, MRI	video, volume